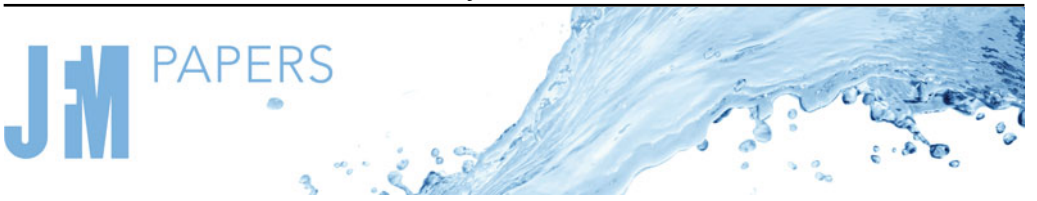
J. Fluid Mech. (2025), *vol.* 1022, A32, doi:10.1017/jfm.2025.10755



Transonic buffet flow adaptive control with time-variant reduced-order model

Chuanqiang Gao[1,2,3], **Xinyu Yang**[1,2,3], **Kai Ren**[1,2,3] **and Weiwei Zhang**[1,2,3]

[1]School of Aeronautics, Northwestern Polytechnical University, Xi'an 710072, PR China

[2]International Joint Institute of Artificial Intelligence on Fluid Mechanics, Northwestern Polytechnical University, Xi'an 710072, PR China

[3]National Key Laboratory of Aircraft Configuration Design, Xi'an 710072, PR China

Corresponding author: Weiwei Zhang, aeroelastic@nwpu.edu.cn

(Received 27 August 2024; revised 15 September 2025; accepted 21 September 2025)

Transonic buffet is a complex and strongly nonlinear unstable flow sensitive to variations in the incoming flow state. This poses great challenges for establishing accurate-enough reduced-order models, limiting the application of model-based control strategies in transonic buffet control problems. To address these challenges, this paper presents a time-variant modelling approach that incorporates rolling sampling, recursive parameter updating and inner iteration strategies under dynamic incoming flow conditions. The results demonstrate that this method successfully overcomes the difficulty in designing appropriate training signals and obtaining unstable steady base flow. Additionally, it improves the global predictive capability and identification efficiency of linear models for nonlinear flow-system responses by more than one order of magnitude. Furthermore, two adaptive control strategies – minimum variance control and generalised predictive control – are validated as effective based on the time-variant reduced-order model through numerical simulations of the transonic buffet flow over the NACA 0012 aerofoil. The adaptive controllers effectively regulate the unstable eigenvalues of the flow system, achieving the desired control outcomes. They ensure that the shock wave buffet phenomenon does not recur after control is applied, and that the actuator deflection, specifically the trailing-edge flap, returns to zero. Moreover, the control results further confirm the global instability essence of transonic buffet flow from a control perspective, thereby deepening the cognition of this nonlinear unstable flow.

Key words: low-dimensional models, control theory, separated flows

https://doi.org/10.1017/jfm.2025.10755 Published online by Cambridge University Press

© The Author(s), 2025. Published by Cambridge University Press.

1. Introduction

1.1. *Transonic buffet flow and its control*

Transonic buffet is a typical and complex unstable flow phenomenon featuring strong unsteadiness and nonlinearity (Caruana *et al.* 2005). The unsteady responses can interact with the structure and cause significant structural vibration, resulting in severe structural fatigue or even flight accidents and restricting the flight envelope of an aeroplane (Dou, Gao & Zhang 2024). Therefore, transonic buffet flow itself and its control have attracted considerable research interest.

This phenomenon was first discovered by Humphreys (1951) in wind tunnels. For a stationary aerofoil in transonic flow, when Mach number Ma and angle of attack α are within a specific range, the upper-surface shock wave will begin self-excited oscillation. This will cause complex shock–boundary-layer interaction and lead to response fluctuations (Tijdeman 1977). A large amount of research has revealed that the physical essence of transonic buffet is the instability of the flow. The early explanation for the inducing mechanism of transonic buffet was a feedback model proposed by Lee (1990). This model assumes that the shock wave oscillation arises from the interaction between the downstreaming pressure wave induced by the shock wave and the upstreaming Kutta wave at the trailing-edge, creating an intricate feedback loop. With the development of global instability theory, Crouch *et al.* (2009) re-examined the physical mechanism of this complex flow phenomenon from the perspectives of flow stability and bifurcation. Through eigenvalue analysis, they found that the transonic buffet characteristics of an aerofoil are determined mainly by the most unstable modes, and accurately predicted the onset boundary and frequency of transonic buffet. This explanation has been increasingly confirmed and recognised by researchers (Jacquin *et al.* 2009; Kuz'min 2009; Sartor, Mettot & Sipp 2015; Dou *et al.* 2024).

Recognising the physical essence of transonic buffet provides great convenience for the following buffet control research. Through linear stability analysis (Sartor *et al.* 2015) and resolvent analysis (Kojima *et al.* 2020; Ma *et al.* 2024; Gao *et al.* 2025*a*; Ma, Gao & Zhang 2025), researchers have found that the shock wave foot and separation bubble at the trailing-edge of an aerofoil are the regions with the strongest sensitivity to control disturbances. Subsequently, the main transonic buffet control strategies can be divided into two categories: intervening in the shock-wave–boundary-layer region or in the trailing-edge flow regions. Passive control methods without energy injection are the main control schemes applied to weaken the shock-wave–boundary-layer interaction (SBLI), such as wavy leading edges (WLEs) (Degregori & Kim 2021), vortex generators (VGs) (Molton *et al.* 2013; Dandois *et al.* 2014, Titchener & Babinsky 2015) and shock control bumps (SCBs) (Mayer *et al.* 2019; Geoghegan, Giannelis & Vio 2020). Meanwhile, the control of flow in the wake region is achieved mostly through active control methods which require extra energy injection, such as trailing-edge devices (TEDs) (Caruana *et al.* 2005; Gao, Zhang & Ye 2016; Tian, Li & Peiqing 2018; Petrocchi, Mauriello & Barakos 2023).

However, existing studies also indicate that the unsteady characteristics of transonic buffet are particularly sensitive to changes in incoming flow conditions (Gao *et al.* 2016; Zhao *et al.* 2020). Especially when the flight attitude changes or encountering disturbances such as gusts, significant nonlinear excitations can be caused, which can lead to nonlinear changes in the characteristics of transonic buffet responses (Friedewald 2023). These changes are unexpected so that the control law designed for a specific incoming flow condition may perform poorly or even have adverse effects under time-variant incoming flow conditions. Only a small amount of research on feedback-loop-embedded closed-loop

https://doi.org/10.1017/jfm.2025.10755 Published online by Cambridge University Press

control demonstrates some but limited condition generalisation capability (Gao *et al.* 2017; Kwon & Vepa 2023; Ren *et al.* 2024). How to design a control law adaptable to these changes in flow condition has become a novel challenge faced by transonic buffet flow control research.

1.2. *Current model-based flow-control design methods*

To achieve good adaptability of closed-loop control for transonic buffet flow under time-variant flow conditions, it is necessary to obtain accurate-enough feedback information for reflecting transient changes in flow characteristics. This actually poses higher requirements for flow modelling, as the majority of current research relies on simplified input–output models of complex flow systems to design the corresponding closed-loop control laws (Galea *et al.* 2003; Sipp & Schmid 2016). Thus, the accuracy of a model determines the effectiveness of the control laws designed based on it. The most commonly used methods for establishing flow models mainly contain flow governing equations, data-driven machine learning and reduced-order modelling techniques.

Firstly, governing-equation-based models, such as direct numerical simulation (DNS) models and linearised Navier–Stokes (NS) equation models (Kim & Bewley 2007; Sipp *et al.* 2010; Tol *et al.* 2017), are derived from the NS equation using discrete and linearisation techniques, aiming to analyse all the physical aspects of complex flow systems. The closed-loop control law designed based on this model is the most physically plausible and has strong interpretability. Recently, resolvent analysis (Herrmann *et al.* 2023; Leclercq & Sipp 2023; Lin, Tsai & Tsai 2023; Nibourel *et al.* 2023; Poulain *et al.* 2024) has promoted the application of governing-equation-based models in control design. However, for flow systems under high Reynolds numbers such as transonic buffet flow, accurate-enough simulation models usually require large amount of grids and huge time consumption. These models also encounter significant computational and storage challenges when employed in closed-loop control design, and the difficulty of modelling also increases exponentially with the growing complexity of the flow system (Brunton & Noack 2015).

On the contrary, models based on data-driven machine learning no longer rely on governing equations (Park & Choi 2020; Li, Li & Noack 2022; Ren *et al.* 2022; Maceda *et al.* 2023; Wang *et al.* 2023*a*). These models take advantage of the nonlinear modelling capabilities of neural networks to directly establish the feedback correlations between the response outputs and the control inputs. For instance, Ren *et al.* (2020) implemented adaptive control of transonic buffet over NACA 0012 aerofoil using radial basis function (RBF) neural networks and found that the designed control law is effective within a certain range of inflow conditions. Peng *et al.* (2020) successfully improved the predictive ability of the nonlinear model for features corresponding to different incoming flow conditions, which can be beneficial for robust control design, by introducing parameters such as Reynolds number Re, aerofoils' geometric features and angles of attack α at the input of convolutional neural networks (CNN). However, since data-driven machine learning models rely entirely on the flow field information covered by the training datasets, it is quite hard for them to guide the control design beyond the knowledge of training datasets, such as guiding the control design of other flow systems that exhibit similar response phenomena but possess significant differences in inherent mechanisms. The strong nonlinearity of neural networks can also lead to high complexity and poor interpretability of the designed control laws. Therefore, despite the great potential demonstrated by machine learning methods, particularly Deep Reinforcement Learning (DRL) (Zhu, Fang & Zhu 2022; Paris, Beneddine & Dandois 2023; Wang *et al.* 2023*b*; Xu & Zhang 2023; Ren *et al.* 2024), in the design of closed-loop control laws, researchers

https://doi.org/10.1017/jfm.2025.10755 Published online by Cambridge University Press

continue to explore adaptive control methods based on simplified and explicit models of complex flows. They target using interpretable models to guide the design of interpretable closed-loop control laws, particularly under time-variant flow conditions.

In comparison with the previous models, reduced-order models (ROMs) more effectively meet the demands of adaptive control design research under time-variant inflow conditions. They not only follow physical principles but also exhibit the ability of deriving key flow characteristics from data (Yang *et al.* 2023; Gao *et al.* 2025*b*). There are currently two main approaches to closed-loop control design based on ROMs (Fabbiane *et al.* 2014), namely 'reduce then design' and 'design then reduce' (Carini, Pralits & Luchini 2015; Semeraro & Pralits 2018). The former has become the most commonly used approach due to its computational cost advantage. It involves establishing a ROM that can reproduce the input–output characteristics of the original system at first, and then carrying out control law design based on the model. This means that the successful design of an effective control law hinges on the ability of the ROM to accurately capture the essential flow characteristics and response evolutions under a specific flow condition or even time-variant conditions. The commonly used methods for establishing ROMs contain modal decomposition methods with feature extraction and system identification methods based on input and output samples. The former can obtain a low-order model composed of several submodes, such as the proper orthogonal decomposition (POD) method (Couplet, Basdevant & Sagaut 2005) and the dynamic mode decomposition (DMD) method (Schmid 2010). The latter can construct a low-order input–output transfer function model of the corresponding complex flow system, such as the Volterra series model (Silva 2005), eigensystem realisation algorithm (ERA) model (Kim *et al.* 2005), autoregressive with exogenous inputs (ARX) model (Zhang & Ye 2007) and so on. These models have been applied successfully to control unstable vortex shedding of a bluff body (Yao & Jaiman 2017), unstable flow in the cavity (Leclercq *et al.* 2019), pulsating loads generated by transonic buffet (Gao *et al.* 2017) and turbulent transition (Dadfar, Hanifi & Henningson 2018). Additionally, the methods in different categories can be combined with each other to better establish ROMs. A typical example is the balanced proper orthogonal decomposition (BPOD) method (Rowley 2005).

Moreover, many researchers have begun to attempt robust adaptive control design with ROMs under different incoming conditions, especially in areas such as flow around a bluff body (Zhang, Cheng & Zhou 2004; Choi, Jeon & Kim 2008; Hasheminejad *et al.* 2014; Stringer, Zang & Hillis 2014; Wang *et al.* 2017; Jussiau *et al.* 2022) and boundary-layer control (Kegerise *et al.* 2007*a*,*b*; Takahashi *et al.* 2011; Fabbiane *et al.* 2015; Tol, Kotsonis & De Visser 2019; Nibourel *et al.* 2024). Among them, some scholars have managed to combine the specific ROMs for typical conditions with adaptive control methods, such as Kegerise *et al.* (2007*a*,*b*). They applied a generalised predictive control (GPC) method based on the specific established ARX models for each of the flow conditions considered in their control experiments and achieved satisfactory multiple Rossiter-mode suppression at fixed Mach numbers. Another approach is to enhance the generalisation of ROMs to provide accurate-enough response predictions for adaptive controllers. For example, Tian, Song & Cattafesta (2006) and Song, Tian & Cattafesta (2007) adopted a recursive system identification (ID) algorithm to estimate the flow dynamics, which does a good job of tracking the unsteady pressure sensor output, thus ensuring the control effectiveness of the disturbance rejection algorithm or GPC method. However, few research has truly demonstrated adaptive control results under the conditions when the incoming flow parameters, such as Ma and α, are continuously varying over time, so-called time-variant incoming flow conditions.

https://doi.org/10.1017/jfm.2025.10755 Published online by Cambridge University Press

Generally speaking, two requirements should be satisfied by the model-based control design method for controlling the unstable flow systems with strong nonlinearity and instability under time-variant incoming flow conditions. Firstly, the flow model needs to change in time. When the flow state changes, the mathematical flow model will also change. The necessity to continuously revise or rebuild the mathematical model brings unpredictable difficulties to control design work. The second is that the control law must adapt to temporal variations. For adaptive control, changes in incoming flow conditions and the flow characteristics necessitate timely adjustments to the control law's parameters, which greatly compounds the difficulty of its design. And there is a coupling relationship between the changes in the model and control law. For example, the feedforward control model established by Nibourel *et al.* (2023) based on a specific incoming condition fails when convective time delays were altered by free-stream velocity variations of ± 5 % due to the inability of upstream sensors to monitor the impact of controller action on flow. The model could not accurately predict the subsequent changes of the flow-control system, resulting in the ineffectiveness of the model-based control law.

1.3. *Objective and outline of the paper*

It is necessary to develop an adaptive control design method that can accurately represent the changes in flow characteristics, enable the acquisition of control parameters, and adapt to time-variant incoming flow conditions. The core challenge behind these requirements is the establishment of an easy-obtaining and accurate-enough ROM.

This article develops a time-variant modelling method with the rolling sampling and recursive parameter updating strategies to improve the global predictive ability and identification efficiency of linear models for unstable flow systems. Section 2 focuses on the analysis of the stability characteristics of the transonic buffet flow over the NACA 0012 aerofoil under time-variant conditions after a brief introduction on the control set-up and the computational fluid dynamics (CFD) simulation method applied in this article. Then § 3 delves into the establishment method of the newly developed time-variant ROM with inner iterations (ITV-ROMs) and exhibits their response predictive ability compared with classical time-invariant ROMs (TI-ROMs) and time-variant ROMs without inner iterations(TV-ROMs). Sections 4 and 5, respectively, introduce two adaptive control strategies, along with their corresponding control effectiveness verification. In § 6, the robustness of the proposed control design method is validated through several complex examples under different time-variant incoming flow conditions. Finally, § 7 offers a summary and outlook.

2. Control problem

This section briefly introduces the control set-up in § 2.1 and the CFD simulation method in § 2.2. Then § 2.3 studies the intrinsic characteristics of transonic buffet flow under time-variant incoming flow conditions. Finally, the adaptive control design framework of this study is outlined in § 2.4.

2.1. *Control set-up*

This study focuses on the transonic buffet flow over the NACA 0012 aerofoil. The active control actuator is a trailing-edge flap with a length of 15 % chord and its rotation axis located at 85 % chord length, as shown in figure 1. Compared with TED, the trailing-edge flap is the original control surface of the wing, eliminating the need to add any additional devices to the system and thereby simplifying the modelling procedure. The closed-loop

https://doi.org/10.1017/jfm.2025.10755 Published online by Cambridge University Press

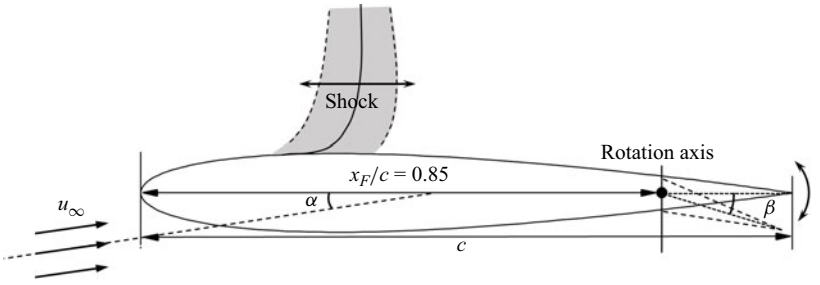


Figure 1. Sketch diagram of NACA 0012 aerofoil and control system.

control takes lift coefficient as the feedback signal. u_∞ represents the free-stream velocity, x_F represents the position of the rotation axis of the trailing edge flap and c is the chord length of the airfoil. As figure 1 illustrates, α is the angle of attack representing the angle between the direction of incoming flow and the chord of the aerofoil, and β is the flap deflection angle showing the angle between the deflected flap and the chord of the aerofoil. The value of α is decided by incoming flow conditions and β is determined by closed-loop control law.

2.2. *CFD simulation*

The numerical simulation of transonic buffet flow is conducted using an in-house hybrid-unstructured flow solver. The finite-volume method is employed to solve the unsteady Reynolds-averaged Navier–Stokes (URANS) equations. The Spalart–Allmaras (SA) turbulence model is applied to close the URANS equations for two-dimensional compressible flow.

The spatial discretisation and time integration of the turbulence model equation and the mean flow equations are weakly coupled. The inviscid flux is discretised by the second-order advection upstream splitting method (AUSM+) and least-squares reconstruction scheme. And the viscous flux is evaluated by the second-order central scheme. The time discretisation uses the dual time stepping method while the pseudo time iteration applies the fourth-stage Runge–Kutta scheme. A detailed introduction to this study's numerical method can be found in Appendix A and Gao *et al.* (2016).

Figure 2 shows the hybrid computational domain of the NACA 0012 aerofoil employed in this study, which is the same as G3 in Gao *et al.* (2016). The far field extends 20 chords from the aerofoil. There are 25 361 surface nodes and 50 layers of the structured viscous grid around the aerofoil. The height of the first boundary layer near the wall is $5 \times 10^{-6}c$ (where c denotes the chord length of the aerofoil), and the non-dimensional wall distance is $y^+ < 1$. The simulation real-time step is $dt_{real} = 2.94 \times 10^{-4}$ s (physical) and the non-dimensional time step is $dt = dt_{real} \times a/c = 0.1$, where a represents the velocity of sound. The chosen Reynolds number throughout this article is $Re = 3 \times 10^6$. As figure 3 shows, the calculated buffet-onset boundary is in good agreement with the experimental results (Doerffer *et al.* 2010). For instance, the simulated buffet-onset angle of attack is approximately 4.8° when $Ma = 0.7$, which is basically consistent with the experimental value of 4.74°. Under this Mach number, the maximum buffet load is obtained at an attack angle of 5.5°. Figure 4 shows the lift coefficient response developing from the unstable steady state to nonlinear limit cycle state and corresponding spectral analysis at $Ma = 0.7$, $\alpha = 5.5°$. The intrinsic Strouhal frequency of the system under this condition is $St = fc/u_\infty = 0.062$, where f is the flow frequency and u_∞ is the free-stream velocity.

https://doi.org/10.1017/jfm.2025.10755 Published online by Cambridge University Press

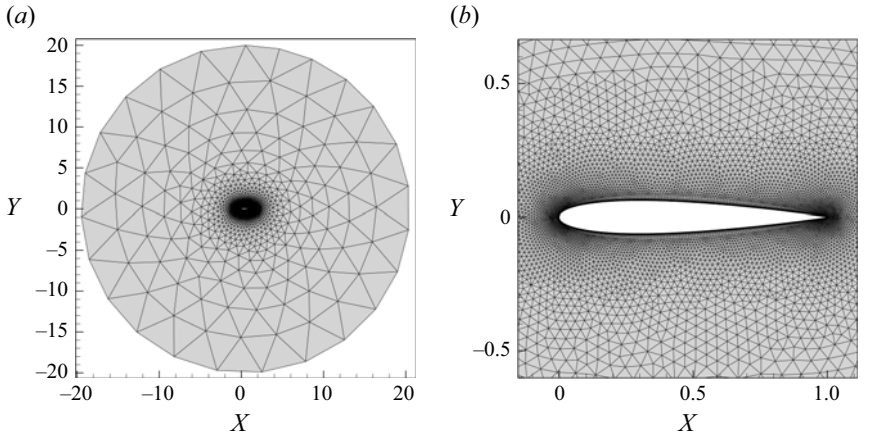


Figure 2. (*a*) Overview of the NACA 0012 aerofoil computational grid and (*b*) detailed mesh around the aerofoil. *X*, *Y* here represent the dimensionless *x* and *y* coordinates.

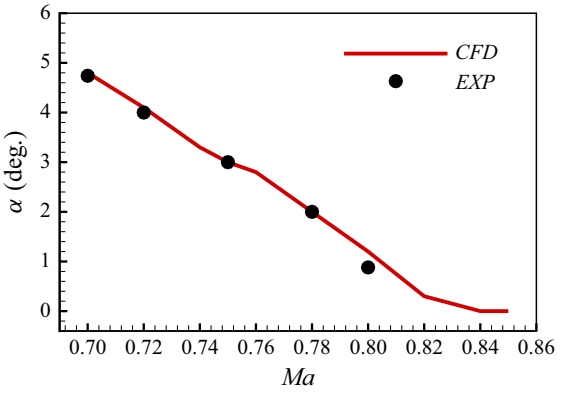


Figure 3. Comparison of buffet-onset boundary.

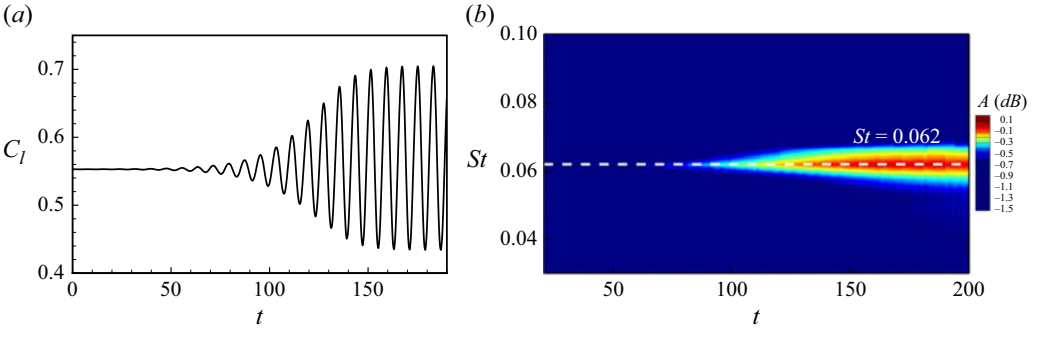


Figure 4. (*a*) Lift response and (*b*) the wavelet analysis of it at $Ma = 0.7$, $\alpha = 5.5°$. C_l is the lift coefficient, and *A* is the amplitude of the wavelet coefficient reflecting the degree of similarity or resonance intensity between the original signal and the wavelet basis function at a specific time and frequency.

https://doi.org/10.1017/jfm.2025.10755 Published online by Cambridge University Press

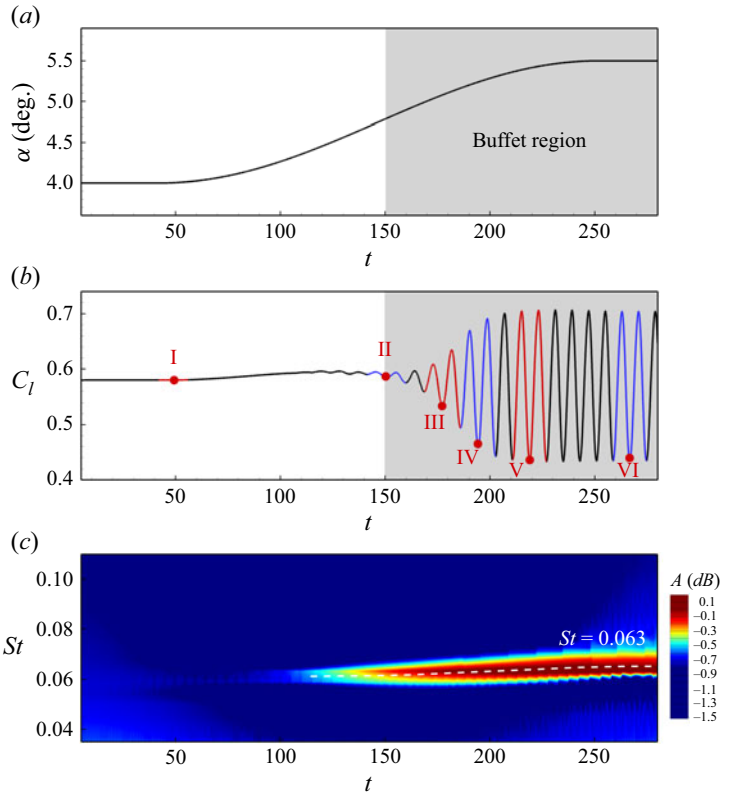


Figure 5. The time-varying characteristics of the transonic buffet flow when $Ma = 0.70$, $\alpha = 4.0° \sim 5.5°$: (*a*) the time-variant incoming flow condition; (*b*) the calculated lift coefficient response and (*c*) the wavelet analysis of the time-varying response.

2.3. *Flow characteristics*

This section examines the time-varying characteristics of the transonic buffet flow under an incoming flow condition when the angle of attack α varies from 4.0° to 5.5° while the Mach number remains constant at 0.70, as illustrated in figure 5(*a*). Through the aforementioned numerical simulation method, the aerodynamic responses of the NACA 0012 aerofoil are obtained, such as the lift coefficient response depicted in figure 5(*b*). Figure 5(*c*) further shows the variation patterns of the dominant frequency of the lift coefficient response under this changing flow condition. The grey area in the figure represents the buffet region. It can be concluded that, as the angle of attack α increases from the non-buffet stage to the buffet stage, the fluctuation amplitude of the aerodynamic response will rise rapidly, and the response frequency will also experience a continuous increase. Moreover, a premature buffet phenomenon may occur attributable to the disturbance caused by the changing condition.

Furthermore, six typical time intervals are selected for conducting DMD modal analysis. The central moments of these intervals are illustrated as red circles in figure 5(*b*) and labelled in chronological sequence. The first three DMD modes, ranked by modal energy, are presented in figure 6, accompanied by the corresponding pressure fields at the representative moments. As observed in figure 6(*a*), the position of the leading shock wave shifts progressively from $P_s = 0.314$ to $P_s = 0.158$ over time, where $P_s = x_s/c$ and x_s represents the chordwise coordinate of the shock wave. The first-order

https://doi.org/10.1017/jfm.2025.10755 Published online by Cambridge University Press

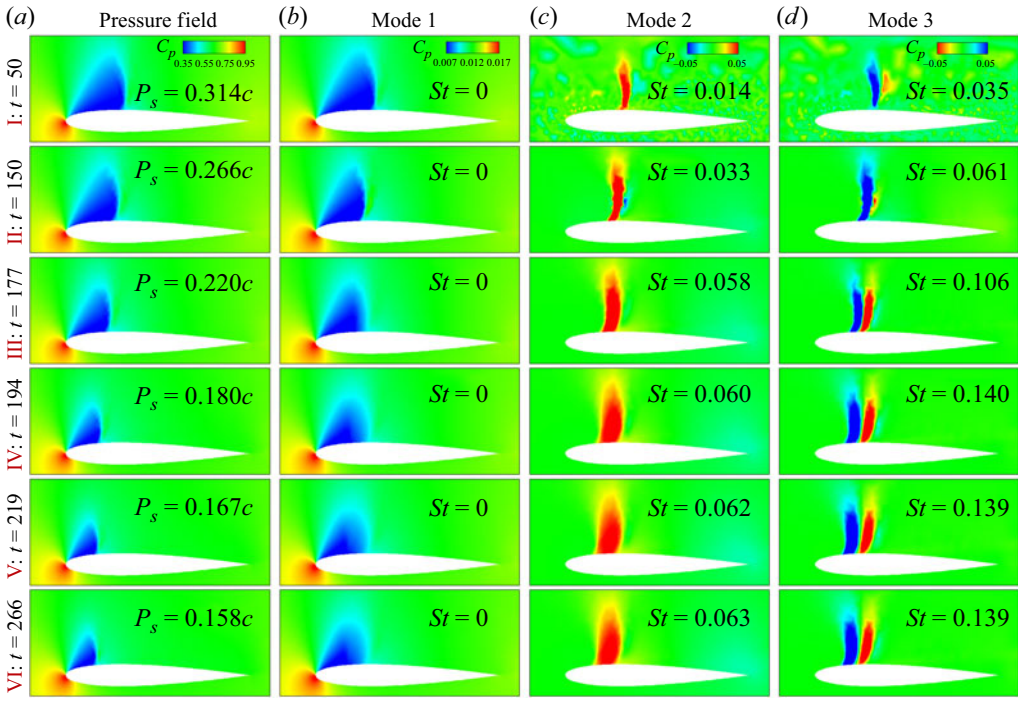


Figure 6. Pressure fields of the time-varying transonic buffet flow and the top three DMD pressure modes at typical moments. C_p here represents the pressure coefficient.

DMD mode corresponds to the zero-frequency time-averaged static mode, whose edge becomes increasingly indistinct, indicating that the flow field undergoes more pronounced variations as time progresses. The remaining modes capture the dynamic features associated with oscillating shock waves. Specifically, the second-order DMD modal frequency gradually converges towards the natural frequency $St = 0.063$ of the transonic buffet flow at $Ma = 0.70$ and $\alpha = 5.5°$, starting from an initial value of $St = 0.014$. Meanwhile, the third-order mode emerges as a harmonic mode of the second-order mode. This observation indicates that the second-order DMD mode corresponds to the main mode of oscillatory shock waves, gradually dominating the transonic buffet flow characteristics over time.

These results strongly demonstrate the sensitivity of the intrinsic characteristics of transonic buffet flow over aerofoils to changes in incoming flow conditions. Meanwhile, the strong nonlinearity of the change in the intrinsic features puts higher demands on the accuracy of aerodynamic modelling and control effectiveness under time-variant incoming flow conditions. Therefore, it is necessary to develop time-variant modelling methods and control design methods for transonic buffet flow under changing conditions.

2.4. *Adaptive control design framework*

The primary existing approach to establishing TV-ROMs is the 'evolve then correct' methodology, where a basic flow evolution model is first established, followed by the development of an error model that captures the discrepancy between time series simulation and the basic model prediction through methods such as neural networks. For example, Pawar *et al.* (2020) employed a recurrent neural network to correct the original intrusive Galerkin model in real time, greatly improving the prediction accuracy

https://doi.org/10.1017/jfm.2025.10755 Published online by Cambridge University Press

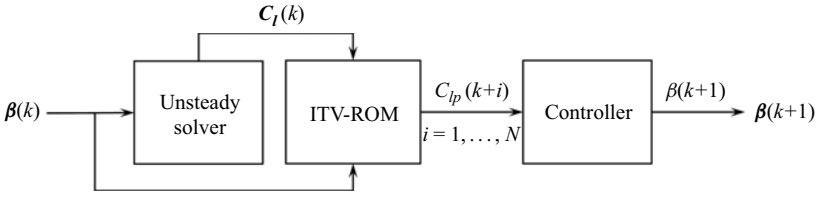


Figure 7. Combination of time-variant modelling and adaptive control design.

of the model. However, the error models introduced to augment model precision often incorporate strong nonlinear terms that are difficult to explicitly represent, posing unpredictable challenges for control design research.

To avoid introducing additional nonlinear terms for error correction, this article develops an ITV-ROM method rooted in the traditional time-invariant modelling architecture, and combines it with adaptive controllers to achieve superior suppression of transonic buffet under time-variant conditions. The parameter update process for time-variant modelling and adaptive control design is shown in figure 7. The data required for updating the parameters of TV-ROMs are the deflection history $\boldsymbol{\beta}(k) = [\beta(k-i), \beta(k-i+1), \ldots, \beta(k)]^{\mathrm{T}}$ of the trailing-edge flap from time step $(k-i)$ to current time step k and the lift response $\boldsymbol{C_l}(k) = [C_l(k-i), C_l(k-i+1), \ldots, C_l(k)]^{\mathrm{T}}$ of the flow system under control. Subsequently, the lift response $C_{lp}(k+i)$, $(i = 1, \ldots, N)$ at time step $(k+i)$ is predicted by the updated model as the input of the adaptive controller. Then the flap deflection angle at the next time step $\beta(k+1)$ is determined by the controller, and the subsequent lift response is calculated using an unsteady CFD solver. By following this process, the adaptive control law design for time-variant flow conditions can be readily achieved.

The two self-tuning control design methods adopted in this article are minimum variance control (MVC) and GPC. The detailed adaptive control design framework is shown in figure 8. The whole design procedure consists of two circuits, which are inner loop A and outer loop B. The inner loop A is composed of a flow system to be controlled and an adjustable controller. The control law generated by the controller acts directly on the flow system. This set-up is quite similar to the traditional feedback loop commonly employed in closed-loop control system. The outer loop B comprises the identification of the ITV-ROM's parameters and the update of the self-tuning controller's parameters, which is the core component of our adaptive control design framework. In this way, the proposed ITV-ROM parameter identification and controller adjustment processes are combined organically to form a real-time control system, thus achieving adaptive control under time-variant incoming flow conditions.

3. Time-variant reduced-order modelling method

The ARX framework is a classical system identification architecture used widely in unsteady aerodynamic modelling and control design of multidisciplinary coupling systems under time-invariant conditions. Section 3.1 provides a general introduction to this architecture, and then § 3.2 emphasises the improvement proposed in this work from TI-ROMs to ITV-ROMs.

3.1. *Traditional time-invariant ARX modelling approach*

The ARX model is usually used to build the aerodynamic ROM (Shi *et al.* 2025), which establishes the transfer function relationship between the input and output data of a complex system based on the following single-input single-output difference equations:

https://doi.org/10.1017/jfm.2025.10755 Published online by Cambridge University Press

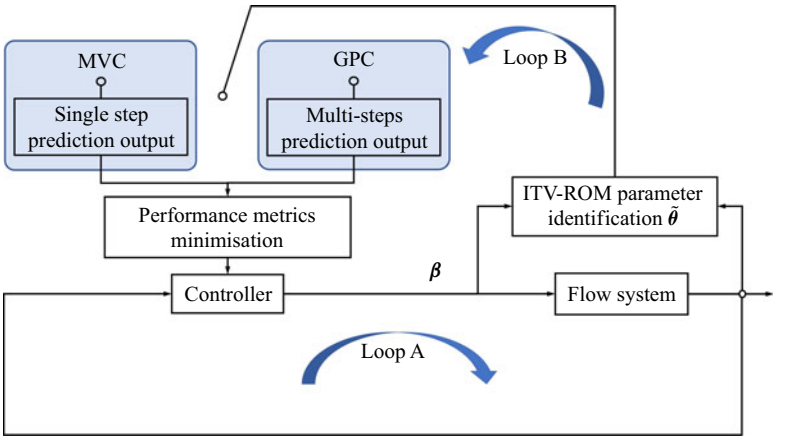


Figure 8. The adaptive control design framework.

$$y(k) = \sum_{i=1}^{na} A_i y(k-i) + \sum_{i=d}^{nb} B_i u(k-i) + \xi(k). \tag{3.1}$$

For this study, $u(k)$ in (3.1) represents the control input, namely, the actuation displacement $\beta(k)$ of the trailing-edge flap; $y(k)$ is the numerical simulated aerodynamic response f_a, such as lift coefficient response C_l, also serving as the feedback signal; and $\xi(k)$ refers to the white noise sequence. Both the input and output data are obtained completely before modelling in this part of work. Here A_i and B_i are the coefficients to be identified offline, where na and nb are the delay orders of the input and output datasets and d is the pure delay between the input and output data, which is taken as $d = 0$ in this study.

Usually, the coefficients are identified through the least-squares (LS) method. Define the parameter matrix $\boldsymbol{\theta}$ and the state vector $\boldsymbol{x}(k)$ as follows:

$$\begin{aligned} \boldsymbol{\theta} &= \left[A_1, \quad \cdots, \quad A_{na}, \quad B_d, \quad \cdots, \quad B_{nb}\right]^{\mathrm{T}}, \\ \boldsymbol{x}(k) &= \left[y(k-1), \quad \cdots, \quad y(k-na), \quad u(k-d), \quad \cdots, \quad u(k-nb)\right]^{\mathrm{T}}. \end{aligned} \tag{3.2}$$

Then (3.1) can be rewritten as

$$y(k) = \boldsymbol{x}^{\mathrm{T}}(k)\boldsymbol{\theta} + \xi(k). \tag{3.3}$$

Assume that there are L couples of input/output data $\{y(k), u(k), k = 1, 2, \ldots, L, L > (na + nb - d + 1)\}$, then the target of the parameter identification process is to minimise the LS criterion J:

$$J = \sum_{k=1}^{L} \xi^2(k) = \sum_{k=1}^{L} \left[y(k) - \boldsymbol{x}^{\mathrm{T}}(k)\tilde{\boldsymbol{\theta}}\right]^2, \tag{3.4}$$

where $\tilde{\boldsymbol{\theta}} = \left[\tilde{A}_1, \quad \cdots, \quad \tilde{A}_{na}, \quad \tilde{B}_d, \quad \cdots, \quad \tilde{B}_{nb}\right]^{\mathrm{T}}$ represents the identified parameter vector.

Further define the following vectors:

$$\begin{aligned} \boldsymbol{Y} &= \left[y(1), \quad y(2), \quad \cdots, \quad y(L)\right]^{\mathrm{T}} \in \mathbb{R}^{L\times 1}, \\ \boldsymbol{E} &= \left[\xi(1), \quad \xi(2), \quad \cdots, \quad \xi(L)\right]^{\mathrm{T}} \in \mathbb{R}^{L\times 1}, \\ \boldsymbol{\Phi}^{\mathrm{T}} &= \left[\boldsymbol{x}(1), \quad \boldsymbol{x}(2), \quad \cdots, \quad \boldsymbol{x}(L)\right] \in \mathbb{R}^{(na+nb-d+1)\times L}. \end{aligned} \tag{3.5}$$

https://doi.org/10.1017/jfm.2025.10755 Published online by Cambridge University Press

Then (3.4) can be turned into

$$\begin{aligned} J &= \boldsymbol{E}^{\mathrm{T}}\boldsymbol{E} \\ &= (\boldsymbol{Y}-\boldsymbol{\Phi}\tilde{\boldsymbol{\theta}})^{\mathrm{T}}(\boldsymbol{Y}-\boldsymbol{\Phi}\tilde{\boldsymbol{\theta}}) \\ &= \boldsymbol{Y}^{\mathrm{T}}\boldsymbol{Y}-2(\boldsymbol{\Phi}^{\mathrm{T}}\boldsymbol{Y})^{\mathrm{T}}\tilde{\boldsymbol{\theta}}+\tilde{\boldsymbol{\theta}}^{\mathrm{T}}\boldsymbol{\Phi}^{\mathrm{T}}\boldsymbol{\Phi}\tilde{\boldsymbol{\theta}}. \end{aligned} \tag{3.6}$$

Make the first derivative of J with respect to $\tilde{\boldsymbol{\theta}}$ equal to 0:

$$\frac{\partial J}{\partial \tilde{\boldsymbol{\theta}}} = -2\boldsymbol{\Phi}^{\mathrm{T}}\boldsymbol{Y}+2\boldsymbol{\Phi}^{\mathrm{T}}\boldsymbol{\Phi}\tilde{\boldsymbol{\theta}} = 0. \tag{3.7}$$

Finally, the parameter vector $\tilde{\boldsymbol{\theta}}$ identified through the LS method is shown as follows:

$$\tilde{\boldsymbol{\theta}} = [\boldsymbol{\Phi}^{\mathrm{T}}\boldsymbol{\Phi}]^{-1}\boldsymbol{\Phi}^{\mathrm{T}}\boldsymbol{Y}, \tag{3.8}$$

where $\boldsymbol{\Phi}$ should be a full column-rank matrix, which requires non-zero input and output data.

Notably, the establishment of (3.1) is based on the assumption that the input and output data of the system satisfy the linear superposition principle. This requires that the acquisition process of the input/output data for linear modelling the transonic buffet system should be constrained within the linear developing stage, imposing stringent requirements on the design of the training signal which serves as both the input data and the external excitation for generating the corresponding output data (Dou *et al.* 2024).

The established ARX model can accurately model the overall dynamic characteristics of the system and be easily changed into discrete state space equations with the help of the state vector $\boldsymbol{x}(k)$ as follows:

$$\begin{cases} \boldsymbol{x}(k+1) = \tilde{\boldsymbol{A}}\boldsymbol{x}(k)+\tilde{\boldsymbol{B}}u(k-d), \\ y(k) = \tilde{\boldsymbol{C}}\boldsymbol{x}(k)+\tilde{B}_d u(k-d), \end{cases} \tag{3.9}$$

where

$$\begin{aligned} \tilde{\boldsymbol{A}} &= \begin{bmatrix} \tilde{A}_1 & \tilde{A}_2 & \cdots & \tilde{A}_{na-1} & \tilde{A}_{na} & 0 & \tilde{B}_{d+1} & \tilde{B}_{d+2} & \cdots & \tilde{B}_{nb-1} & \tilde{B}_{nb} \\ 1 & 0 & \cdots & 0 & 0 & 0 & 0 & 0 & \cdots & 0 & 0 \\ \vdots & 1 & \cdots & 0 & 0 & 0 & 0 & 0 & \cdots & 0 & 0 \\ \vdots & \vdots & \ddots & \vdots & \vdots & \vdots & \vdots & \vdots & \ddots & \vdots & \vdots \\ 0 & 0 & \cdots & 1 & 0 & 0 & 0 & 0 & \cdots & 0 & 0 \\ 0 & 0 & \cdots & 0 & 1 & 0 & 0 & 0 & \cdots & 0 & 0 \\ 0 & 0 & \cdots & 0 & 0 & 0 & 0 & 0 & \cdots & 0 & 0 \\ 0 & 0 & \cdots & 0 & 0 & 0 & 1 & 0 & \cdots & 0 & 0 \\ 0 & 0 & \cdots & 0 & 0 & 0 & 0 & 1 & \cdots & 0 & 0 \\ \vdots & \vdots & \ddots & \vdots & \vdots & \vdots & \vdots & \vdots & \ddots & \vdots & \vdots \\ 0 & 0 & \cdots & 0 & 0 & 0 & 0 & 0 & \cdots & 1 & 0 \end{bmatrix}, \\ \tilde{\boldsymbol{B}} &= \begin{bmatrix} \tilde{B}_d & 0 & \cdots & 0 & 1 & 0 & 0 & \cdots & 0 \end{bmatrix}^{\mathrm{T}}, \\ \tilde{\boldsymbol{C}} &= \begin{bmatrix} \tilde{A}_1 & \tilde{A}_2 & \cdots & \tilde{A}_{na-1} & \tilde{A}_{na} & 0 & \tilde{B}_{d+1} & \tilde{B}_{d+2} & \cdots & \tilde{B}_{nb-1} & \tilde{B}_{nb} \end{bmatrix}. \end{aligned} \tag{3.10}$$

https://doi.org/10.1017/jfm.2025.10755 Published online by Cambridge University Press

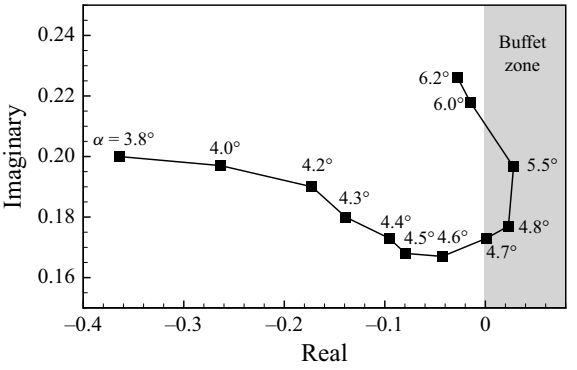


Figure 9. Flow characteristic modes predicted by ARX model at different angles of attack when $Ma = 0.7$.

Subsequently, the discrete-time form equations can be further turned into the continuous-time form shown through bilinear transformation as follows:

$$\begin{cases} \dot{\boldsymbol{x}}(t) = \boldsymbol{A}\boldsymbol{x}(t) + \boldsymbol{B}u(t - t_0), \\ y(t) = \boldsymbol{C}\boldsymbol{x}(t) + B_d u(t - t_0). \end{cases} \tag{3.11}$$

$\boldsymbol{A}$, $\boldsymbol{B}$, $\boldsymbol{C}$ are the coefficient matrices of the continuous-time form equations. t represents the continuous time and t_0 is the continuous time delay between the input and output signal. Figure 9 shows the distribution of dominant eigenvalues of the matrix $\boldsymbol{A}$ at different angles of attack when $Ma = 0.7$. The sign of the real part of the dominant eigenvalues represents the stability characteristics of the flow system. When it is positive, the flow system is unstable along with the appearance of the transonic shock buffet phenomenon, and vice versa. From the figure 9, it can be concluded that the model-predicted buffet-onset and offset angles of attack are approximately 4.8° and 6°, respectively, which are consistent with the CFD calculation results and the experimental results (Doerffer *et al.* 2010) shown in figure 3, validating that the modelling accuracy is satisfactory.

Consequently, the aforementioned offline modelling method has been widely combined with model-based control design methods under time-invariant incoming flow conditions, achieving satisfactory control effects (Gao *et al.* 2017).

3.2. *Inner-iterated time-variant reduced-order modelling method*

However, for the adaptive control under time-variant conditions, the former established TI-ROM fails to provide accurate-enough aerodynamic prediction when the incoming flow conditions change, as it is difficult for designing an appropriate training signal or establishing a universal linear model for the system with time-variant intrinsic features, let alone correctly guide the flap's actuation and achieve the control objectives.

To improve the high-precision prediction ability of the model under time-variant conditions and achieve the goal of overcoming the existing limitations of time-invariant models, this study develops a time-variant reduced-order modelling method based on the idea of local linearisation. With the ARX modelling architecture remaining unchanged, this method updates the model parameters online by rolling sampling the input/output data and applying the recursive least-square (RLS) method instead of the LS method introduced in § 3.1, simultaneously reducing the storage occupation. Figure 10 briefly introduces the sampling difference between the two modelling methods.

https://doi.org/10.1017/jfm.2025.10755 Published online by Cambridge University Press

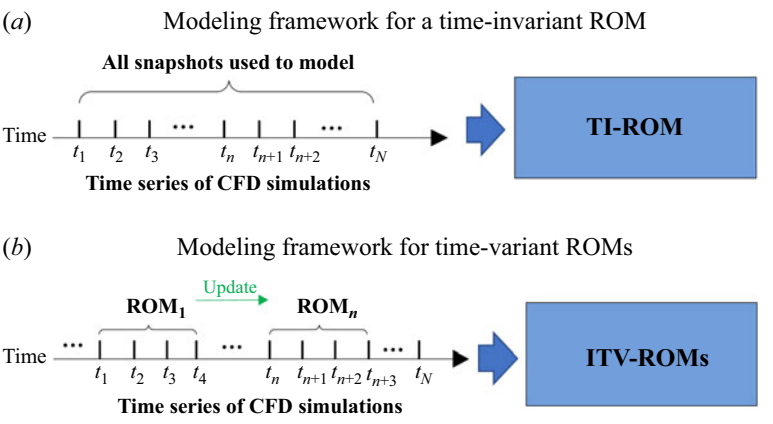


Figure 10. Comparison of the two modelling frameworks.

The main idea of the RLS method is to transform the standard LS estimation equation (3.8) into the recursive form shown in the following expression (Pang & Cui 2013):

$$\tilde{\boldsymbol{\theta}}(k) = \tilde{\boldsymbol{\theta}}(k-1) + \boldsymbol{\theta}_{\xi}(k), \tag{3.12}$$

where $\tilde{\boldsymbol{\theta}}(k)$ represents the identified parameter matrix of the ROM at discrete time step k and $\boldsymbol{\theta}_{\xi}(k)$ is the correction term between the parameter matrices of the adjacent two steps $(k-1)$ and k.

Assume the identified parameter matrix at time step k can be written as

$$\tilde{\boldsymbol{\theta}}(k) = \left[\boldsymbol{\Phi}^{\mathrm{T}}(k)\boldsymbol{\Phi}(k)\right]^{-1}\boldsymbol{\Phi}^{\mathrm{T}}(k)\boldsymbol{Y}(k), \tag{3.13}$$

where

$$\begin{aligned} \boldsymbol{\Phi}(k) &= \begin{bmatrix} \boldsymbol{\Phi}(k-1) \\ \boldsymbol{x}^{\mathrm{T}}(k) \end{bmatrix} \in \mathbb{R}^{k\times(na+nb-d+1)}, \\ \boldsymbol{Y}(k) &= \begin{bmatrix} \boldsymbol{Y}(k-1) \\ y(k) \end{bmatrix} \in \mathbb{R}^{k\times 1}. \end{aligned} \tag{3.14}$$

Define

$$\begin{aligned} \boldsymbol{P}(k) &= [\boldsymbol{\Phi}^{\mathrm{T}}(k)\boldsymbol{\Phi}(k)]^{-1} \\ &= [\boldsymbol{\Phi}^{\mathrm{T}}(k-1)\boldsymbol{\Phi}(k-1) + \boldsymbol{x}(k)\boldsymbol{x}^{\mathrm{T}}(k)]^{-1} \\ &= [\boldsymbol{P}^{-1}(k-1) + \boldsymbol{x}(k)\boldsymbol{x}^{\mathrm{T}}(k)]^{-1}, \end{aligned} \tag{3.15}$$

then

$$\boldsymbol{P}^{-1}(k) = \boldsymbol{P}^{-1}(k-1) + \boldsymbol{x}(k)\boldsymbol{x}^{\mathrm{T}}(k). \tag{3.16}$$

Substitute (3.16) into (3.13):

$$\begin{aligned} \tilde{\boldsymbol{\theta}}(k) &= [\boldsymbol{\Phi}^{\mathrm{T}}(k)\boldsymbol{\Phi}(k)]^{-1}\boldsymbol{\Phi}^{\mathrm{T}}(k)\boldsymbol{Y}(k) \\ &= \boldsymbol{P}(k)\boldsymbol{\Phi}^{\mathrm{T}}(k)\boldsymbol{Y}(k) \\ &= \boldsymbol{P}(k)[\boldsymbol{\Phi}^{\mathrm{T}}(k-1)\boldsymbol{Y}(k-1) + \boldsymbol{x}(k)y(k)] \\ &= \boldsymbol{P}(k)[\boldsymbol{P}^{-1}(k-1)\tilde{\boldsymbol{\theta}}(k-1) + \boldsymbol{x}(k)y(k)] \\ &= \boldsymbol{P}(k)\{[\boldsymbol{P}^{-1}(k) - \boldsymbol{x}(k)\boldsymbol{x}^{\mathrm{T}}(k)]\tilde{\boldsymbol{\theta}}(k-1) + \boldsymbol{x}(k)y(k)\} \end{aligned}$$

https://doi.org/10.1017/jfm.2025.10755 Published online by Cambridge University Press

$$\begin{aligned}&= \tilde{\boldsymbol{\theta}}(k-1) - \boldsymbol{P}(k)\boldsymbol{x}(k)\boldsymbol{x}^{\mathrm{T}}(k)\tilde{\boldsymbol{\theta}}(k-1) + \boldsymbol{P}(k)\boldsymbol{x}(k)y(k)\\ &= \tilde{\boldsymbol{\theta}}(k-1) + \boldsymbol{P}(k)\boldsymbol{x}(k)[y(k) - \boldsymbol{x}^{\mathrm{T}}(k)\tilde{\boldsymbol{\theta}}(k-1)].\end{aligned} \tag{3.17}$$

Further define

$$\boldsymbol{K}(k) = \boldsymbol{P}(k)\boldsymbol{x}(k). \tag{3.18}$$

Based on the matrix inverse lemma

$$(\boldsymbol{A} + \boldsymbol{BC})^{-1} = \boldsymbol{A}^{-1} - \boldsymbol{A}^{-1}\boldsymbol{B}(\boldsymbol{I} + \boldsymbol{CA}^{-1}\boldsymbol{B})^{-1}\boldsymbol{CA}^{-1}, \tag{3.19}$$

where the matrices $\boldsymbol{A}$, $(\boldsymbol{A} + \boldsymbol{BC})$ and $(\boldsymbol{I} + \boldsymbol{CA}^{-1}\boldsymbol{B})$ are required to be non-singular, we can let $\boldsymbol{A} = \boldsymbol{P}^{-1}(k-1)$, $\boldsymbol{B} = \boldsymbol{x}(k)$ and $\boldsymbol{C} = \boldsymbol{x}^{\mathrm{T}}(k)$ and obtain

$$\boldsymbol{P}(k) = \boldsymbol{P}(k-1) - \boldsymbol{P}(k-1)\boldsymbol{x}(k)[1 + \boldsymbol{x}^{\mathrm{T}}(k)\boldsymbol{P}(k-1)\boldsymbol{x}(k)]^{-1}\boldsymbol{x}^{\mathrm{T}}(k)\boldsymbol{P}(k-1). \tag{3.20}$$

Take (3.20) back into (3.18):

$$\begin{aligned}\boldsymbol{K}(k) &= \boldsymbol{P}(k-1)\boldsymbol{x}(k) - \frac{\boldsymbol{P}(k-1)\boldsymbol{x}(k)\boldsymbol{x}^{\mathrm{T}}(k)\boldsymbol{P}(k-1)\boldsymbol{x}(k)}{1 + \boldsymbol{x}^{\mathrm{T}}(k)\boldsymbol{P}(k-1)\boldsymbol{x}(k)}\\ &= \frac{\boldsymbol{P}(k-1)\boldsymbol{x}(k)[1 + \boldsymbol{x}^{\mathrm{T}}(k)\boldsymbol{P}(k-1)\boldsymbol{x}(k)] - \boldsymbol{P}(k-1)\boldsymbol{x}(k)\boldsymbol{x}^{\mathrm{T}}(k)\boldsymbol{P}(k-1)\boldsymbol{x}(k)}{1 + \boldsymbol{x}^{\mathrm{T}}(k)\boldsymbol{P}(k-1)\boldsymbol{x}(k)}\\ &= \frac{\boldsymbol{P}(k-1)\boldsymbol{x}(k)}{1 + \boldsymbol{x}^{\mathrm{T}}(k)\boldsymbol{P}(k-1)\boldsymbol{x}(k)},\\ \boldsymbol{P}(k) &= [\boldsymbol{I} - \boldsymbol{K}(k)\boldsymbol{x}^{\mathrm{T}}(k)]\boldsymbol{P}(k-1).\end{aligned} \tag{3.21}$$

Until now, the RLS-based parameter identification process can be concluded as the following set of equations:

$$\begin{cases}\tilde{\boldsymbol{\theta}}(k) = \tilde{\boldsymbol{\theta}}(k-1) + \boldsymbol{K}(k)[y(k) - \boldsymbol{x}^{\mathrm{T}}(k)\tilde{\boldsymbol{\theta}}(k-1)],\\ \boldsymbol{K}(k) = \dfrac{\boldsymbol{P}(k-1)\boldsymbol{x}(k)}{1 + \boldsymbol{x}^{\mathrm{T}}(k)\boldsymbol{P}(k-1)\boldsymbol{x}(k)},\\ \boldsymbol{P}(k) = [\boldsymbol{I} - \boldsymbol{K}(k)\boldsymbol{x}^{\mathrm{T}}(k)]\boldsymbol{P}(k-1).\end{cases} \tag{3.22}$$

To ensure that the ITV-ROM exhibits satisfactory accuracy at each time step, this study further introduces an inner iteration into the parameter update process. During the inner iteration, the model parameters are still updated by (3.22) with the input and output data unchanged until the following convergence criterion is met within each time step k:

$$\Delta\tilde{\boldsymbol{\theta}}_k = \tilde{\boldsymbol{\theta}}_k(m) - \tilde{\boldsymbol{\theta}}_k(m-1) \leqslant \boldsymbol{\epsilon}, \tag{3.23}$$

where $m \leqslant 100$ is the number of inner iterations for time step k, and $\boldsymbol{\epsilon}$ is a sufficiently small vector with all positive real elements set to 10^{-6} in this paper.

This study activates the recursive formula through manually assigning the initial matrices as follows:

$$\begin{cases}\boldsymbol{P}(0) = p\boldsymbol{I},\\ \tilde{\boldsymbol{\theta}}(0) = \boldsymbol{\epsilon},\end{cases} \tag{3.24}$$

where p is a sufficiently large positive real number with a magnitude between 10^4 and 10^{10}.

https://doi.org/10.1017/jfm.2025.10755 Published online by Cambridge University Press

Incoming flow conditions		Time-invariant condition $\alpha = 5.5°$						Time-variant condition $\alpha = 4.0° \sim 5.5°$		
Training signals		A			B			C	D	E
TI-ROM	Orders ($na = nb$)	40	80	160	40	80	160	40	40	—
	Error (%)	16.24	26.99	458.56	111.81	105.43	92.02	118.12	99.01	—
	Total CPU time (s)	0.95	1.77	1.56	1.73	1.61	12.34	2.11	2.05	—
TV-ROM	Orders ($na = nb$)	4	8	16	4	8	16	4	4	4
	Error (%)	21.50	18.69	17.78	3.77	2.50	1.67	0.85	1.16	0.81
	Total CPU time (s)	0.00	0.00	0.016	0.00	0.030	0.020	0.031	0.031	0.031
ITV-ROM	Orders ($na = nb$)	4	8	16	4	8	16	4	4	4
	Error (%)	4.66	3.32	2.22	0.40	0.31	0.29	0.081	0.089	0.079
	Total CPU time (s)	0.22	0.17	0.30	0.27	0.30	0.55	0.31	0.41	0.41

Table 1. Comparison of modelling accuracy and computational efficiency across different ROM methods with different orders under different incoming flow conditions and training signals when $Ma = 0.70$.

3.3. *Comparison of the two modelling methods*

This section further compares the identification ability of different modelling methods. The definition of the identification error is as follows:

$$Error(\%) = \frac{\sum_{k=1}^{N} | y(k) - \tilde{y}(k) |}{\sum_{k=1}^{N} | y(k) |}, \tag{3.25}$$

where $\tilde{y}(k)$ represents the response reversed by the ROM at time step k, which is chosen as the lift coefficient response C_l throughout the following study, and N is the length of the input/output data. According to experience (Li, Zhang & Gao 2018; Dou *et al.* 2024; Gao *et al.* 2025*b*), the ARX model has a relatively high identification accuracy when $na = nb$. Thus, this article considers only the case of $na = nb$ when identifying the model.

We designed five different training signals to test the identification ability and efficiency of TI-ROMs, TV-ROMs and ITV-ROMs under the previously introduced conditions, with the results depicted in table 1 and figure 11. Among them, signals A and B are used for the time-invariant buffet condition shown in figure 4, while signals C, D and E are meant for the time-variant condition shown in figure 5(*a*).

Both signals A and B act on the unstable steady base flow to ensure the stimulated unstable system remains at a linear developing stage as long as possible, thus enabling the TI-ROMs to work well. Signal A features constant amplitude and varying frequency within the range of $0.05 \leqslant St \leqslant 0.30$, and its length is shorter than that of the linear developing stage of the flow system. Signal B is a signal formed by concatenating signal A with a zero signal, making the system freely develop to the nonlinear stage after the external excitation ends. The analysis of the output lift response stimulated by signal B is shown in figure 12.

Signal C is the superposition of two pulse signals with different amplitudes. The pulse signal with an amplitude of 0.2° acts on the stable flow state of $Ma = 0.7$, $\alpha = 4.0°$, while the pulse signal with an amplitude of 0.4° acts on the buffet state. Signal D shares the same frequency with the transonic buffet flow over the NACA 0012 aerofoil at $Ma = 0.7$, $\alpha = 5.5°$ and its amplitude increases linearly from 0.2° to 0.5°. Signal E is a zero signal.

Table 1 systematically presents the identification error and time consumption of different modelling methods under different incoming flow conditions, training signals and delay orders. It can be seen that the TI-ROMs have good identification accuracy only

https://doi.org/10.1017/jfm.2025.10755 Published online by Cambridge University Press

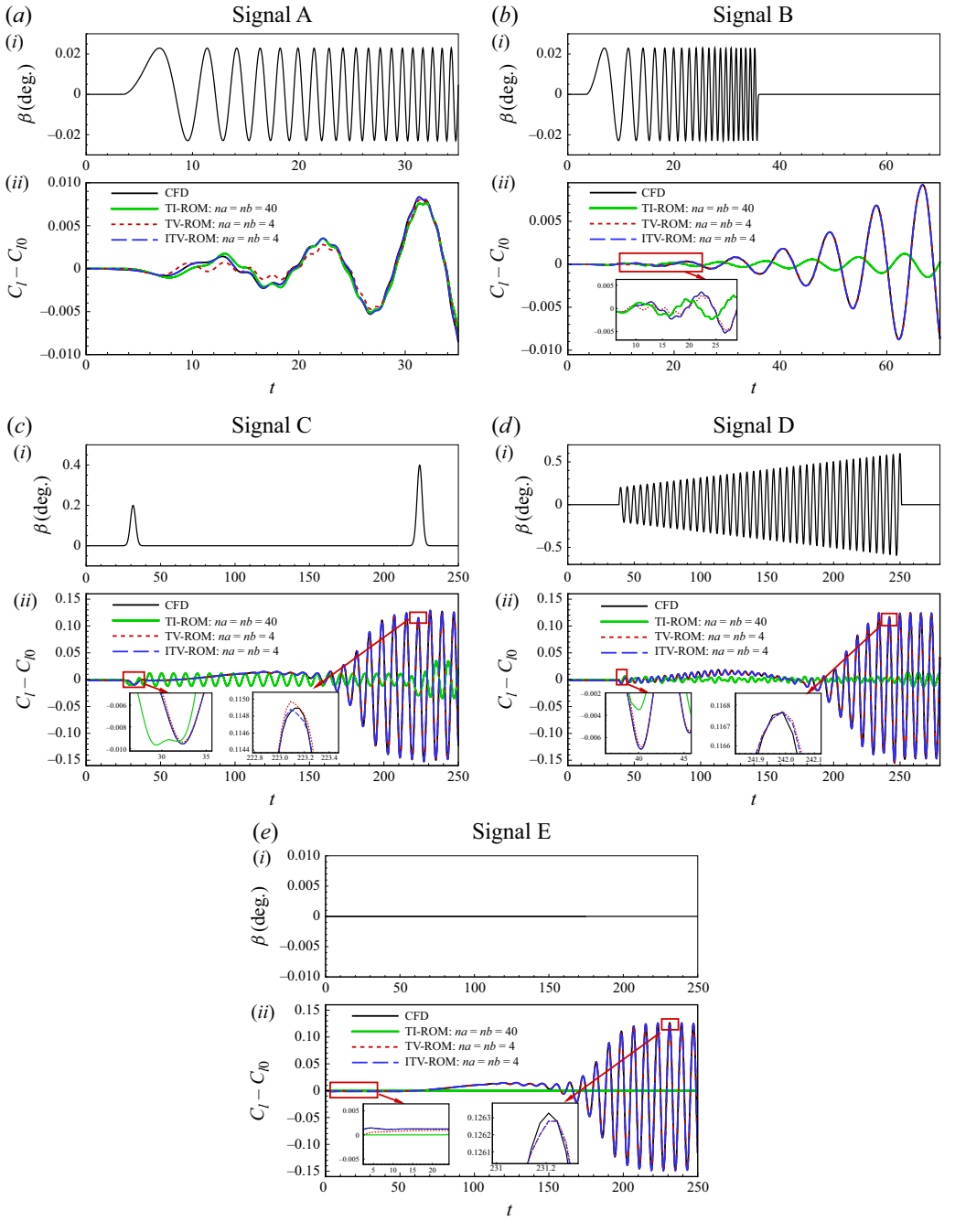


Figure 11. Comparison of the identified responses under different incoming flow conditions and training signals.

when the proportion of non-zero signals is large enough and the flow system remains at a linear developing stage under time-invariant conditions. The TV-ROMs can stabilise the identification accuracy within 5 % when the signal length is long enough as it takes time for the parameters of TV-ROM to converge to the real system parameters. In comparison,

https://doi.org/10.1017/jfm.2025.10755 Published online by Cambridge University Press

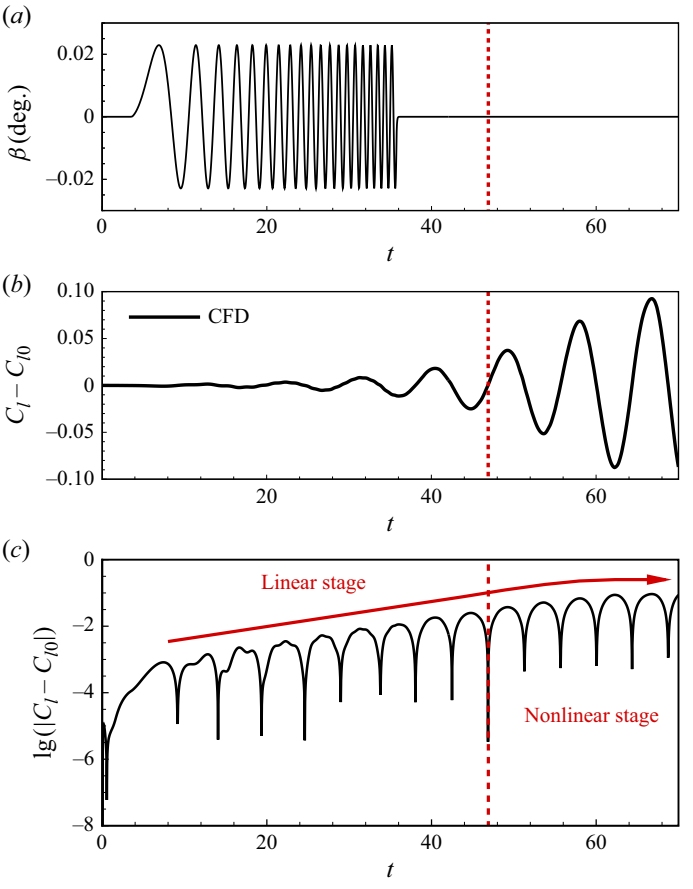


Figure 12. Analysis of the response developing process from the unstable steady base flow with the excitation of training signal B at $Ma = 0.7$, $\alpha = 5.5°$.

the ITV-ROMs show the highest identification accuracy under various inflow conditions and training signals. At the same time, both TV-ROMs require a very small delay order, which is approximately 0.1 times that of the TI-ROMs, greatly reducing the storage usage and thus significantly improving the identification efficiency.

Figure 11 further exhibits the identification results, where the initial unstable steady lift coefficient C_{l0} of time-invariant condition is 0.5529 and the stable lift coefficient of time-variant condition is $C_{l0} = 0.5798$. It can be concluded that the TV-ROMs have overcome the problem of linear models being unable to predict the response history of transition and nonlinear limit cycles. Meanwhile, the parameter update method with recursive characteristics also enables the TV-ROMs to perform response prediction work with zero input.

Table 2 concludes the improvement of the ITV-ROMs compared with the TI-ROMs. As it illustrates, the ITV-ROMs improve the global predictive ability of the linear model for nonlinear flow-system response through a rolling sampling strategy and RLS-based parameter update strategy. They also significantly reduce the amount of storage occupied in the model identification process, improve identification efficiency, and provide new possibilities for feedback control design work combined with model-based adaptive control methods. As four-order ITV-ROM is accurate enough in response prediction, so this study fixes the orders of ITV-ROM as $na = nb = 4$.

https://doi.org/10.1017/jfm.2025.10755 Published online by Cambridge University Press

Model	TI-ROM	ITV-ROM
Input signals	Non-zero and strictly designed	Random
Base flow field	Unstable steady base flow with high accuracy	Random
Data sampling method	Offline sampling	Online rolling sampling
Output responses	Within linear developing stage	Random
Parameter identification method	LS	RLS
Identifiable condition	Time-invariant inflow conditions	Random

Table 2. Improvement of the ITV-ROMs compared with the TI-ROMs.

4. ITV-ROM-based MVC

Minimum variance control is an comprehensive and easy implementing adaptive control method. Section 4.1 introduces the procedure of implementing this method and § 4.2 shows the influence of different target outputs and validates the effectiveness of the control law guided by MVC.

4.1. *Methodology of MVC*

Minimum variance control is designed with the goal of minimising output variance. Due to the delay normally existing in dynamics systems, assuming a delay of d, the current control may make an effect on the system output after d sampling time steps. Therefore, in order to minimise the output variance, it is necessary to make predictions on the output in advance, and then design the required control law based on the predicted values obtained. By continuously predicting and conducting control instructions, it is possible to ensure that the steady-state output variance is minimised. It can be seen that the key to achieving MVC lies in the accuracy of output prediction.

The specific steps of MVC are as follows. To begin with, the difference equations shown in (3.1) need to be transformed into a discrete-time form using the z-transform, demonstrated as follows with the assumption of $\xi(k) = 0$:

$$A(z^{-1})y(k) = z^{-d}B(z^{-1})u(k). \tag{4.1}$$

The parameters of the coefficient matrices can be obtained through the RLS method introduced in § 3.2, the representations of which are as follows:

$$\begin{cases} A(z^{-1}) = 1 - A_1 z^{-1} - A_2 z^{-2} - \cdots - A_{na} z^{-na}, \\ B(z^{-1}) = B_d + B_{d+1} z^{-1} + B_{d+2} z^{-2} + \cdots + B_{nb} z^{-nb+d},\ B_d \neq 0. \end{cases} \tag{4.2}$$

Calculate the future output $\tilde{y}(k+d|k)$ at time step $(k+d)$ predicted by the ITV-ROM established at time step k as the preparation of the control law design process. The control target applied in this section is to minimise the variance between the predicted output and the expected output, with the performance metric J shown as follows:

$$J = \mathbf{E}\left\{[\tilde{y}(k+d) - y_r(k+d)]^2\right\}. \tag{4.3}$$

Here, $y_r(k+d)$ is the target output defined by the researcher based on the system characteristics, which can be the mean system response or the unstable steady response solution.

According to the optimal control requirements, if targeting at minimising the performance metric J, the MVC law can be obtained as follows:

$$F(z^{-1})u(k) = y_r(k+d) - G(z^{-1})y(k), \tag{4.4}$$

https://doi.org/10.1017/jfm.2025.10755 Published online by Cambridge University Press

Algorithm 1 algorithm of MVC

Initialise: $\tilde{\boldsymbol{\theta}}(0)$, $\boldsymbol{P}(0)$ for RLS,
Input: control stop time t_{stop}; model parameters na, nb and d,
1: **for** each $k \in [1, t_{stop}]$ **do**
2: Sample current output $y(k)$ and target output $y_r(k+d)$,
3: Use RLS to get the parameter matrix's estimation $\tilde{\boldsymbol{\theta}}(k)$, namely $A(z^{-1})$ and $B(z^{-1})$,
4: Solve the coefficients of the polynomials $E(z^{-1})$, $F(z^{-1})$ and $G(z^{-1})$ according to (4.5),
5: Execute $u(k)$ according to (4.4).
6: **end for**

where

$$\begin{cases} 1 = A(z^{-1})E(z^{-1}) + z^{-d}G(z^{-1}), \\ F(z^{-1}) = B(z^{-1})E(z^{-1}), \end{cases} \tag{4.5}$$

and

$$\begin{cases} E(z^{-1}) = 1 + e_1 z^{-1} + e_2 z^{-2} + \cdots + e_{ne} z^{-ne}, \ (ne = d-1) \\ G(z^{-1}) = g_0 + g_1 z^{-1} + g_2 z^{-2} + \cdots + g_{ng} z^{-ng}, \ (ng = na-1) \\ F(z^{-1}) = f_0 + f_1 z^{-1} + f_2 z^{-2} + \cdots + f_{nf} z^{-nf}, \ (nf = nb + d - 1). \end{cases} \tag{4.6}$$

Similar to $A(z^{-1})$ and $B(z^{-1})$, $E(z^{-1})$, $F(z^{-1})$, and $G(z^{-1})$ are also polynomials obtained through z-transform, where e_i, f_i, g_i are the coefficients awaiting to be solved through (4.5). ne, ng, nf are the orders of these polynomials, respectively.

The whole MVC algorithm can be concluded as Algorithm 1.

Notably, take (4.1) into (4.4) and then the expression of the input and the output can be turned into

$$\begin{cases} u(k) = \dfrac{\dfrac{1}{F}}{1 + \dfrac{z^{-d}B}{A}\dfrac{G}{F}} y_r(k+d) + \dfrac{-\dfrac{1}{A}\dfrac{G}{F}}{1 + \dfrac{z^{-d}B}{A}\dfrac{G}{F}} \xi(k) = \dfrac{A y_r(k+d) - G\xi(k)}{B}, \\ y(k) = \dfrac{z^{-d}B}{A} u(k) + \dfrac{1}{A}\xi(k) = y_r(k) + E\xi(k), \end{cases} \tag{4.7}$$

where A, B, E, F and G are the abbreviations of $A(z^{-1})$, $B(z^{-1})$, $E(z^{-1})$, $F(z^{-1})$ and $G(z^{-1})$. It can be concluded that the essence of MVC is to use the pole of the controller (the zero of $F(z^{-1})$) to cancel the zero of the controlled object (the zero of $B(z^{-1})$). According to (4.7), when $B(z^{-1})$ is unstable, the control input $u(k)$ will increase exponentially and reach the saturation, eventually resulting in the instability of the flow-control coupled system (Sipp & Schmid 2016).

Unfortunately, the controlled object of this study shows a great potential in having unstable zeros of $B(z^{-1})$ as the transonic buffet flow system itself is a highly nonlinear system with strong instability. Figure 13 shows the trajectories of the zeros of $B(z^{-1})$ obtained through the ITV-ROM under the condition shown in figure 5. It is obvious that when the shock wave buffet phenomenon begins to occur, the stable zeros of $B(z^{-1})$ quickly change to unstable ones (changing from inside the black stable boundary to outside). Therefore, it is necessary to take certain actions on the choice of the expected output $y_r(k+d)$ to overcome the influence of the existing unstable zeros of $B(z^{-1})$ when applying ITV-ROM-based MVC method for closed-loop control design.

https://doi.org/10.1017/jfm.2025.10755 Published online by Cambridge University Press

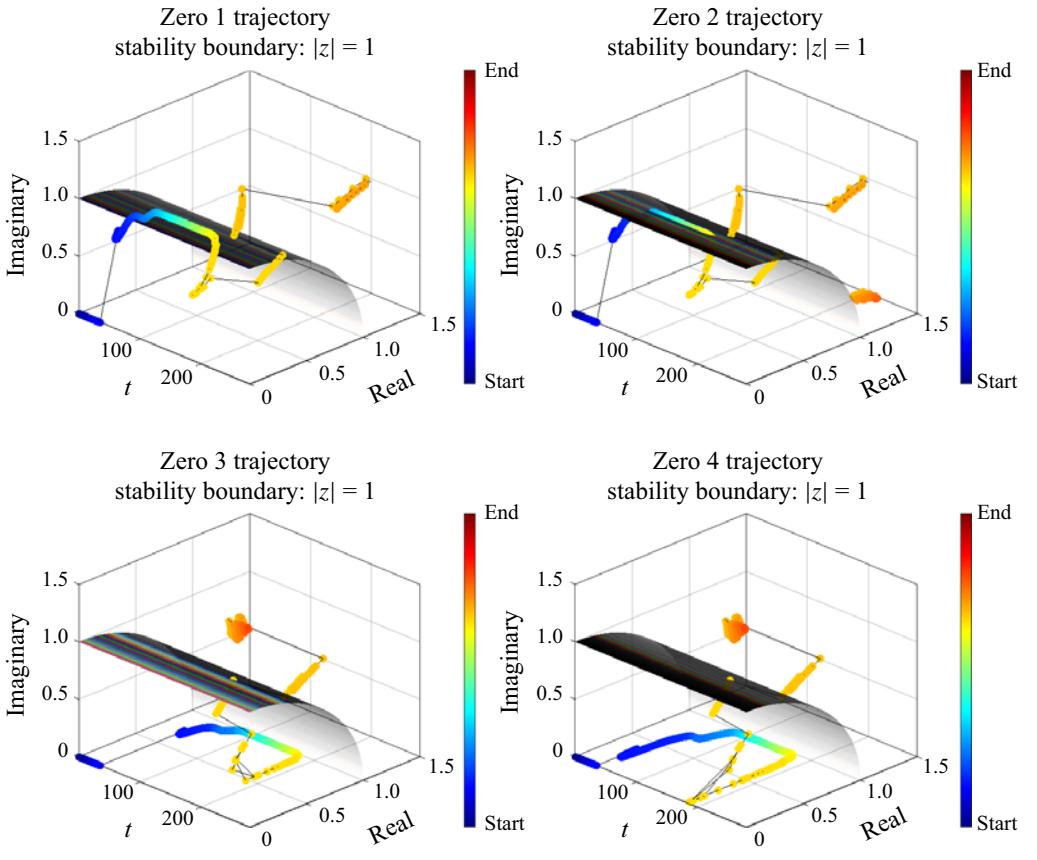


Figure 13. The trajectories of the zeros of $B(z^{-1})$ under the time-variant condition when $Ma = 0.70$, $\alpha = 4.0° \sim 5.5°$.

4.2. *MVC for transonic buffet*

In the numerical simulation environment, it can be approximately assumed that the transonic buffet flow response has no significant delay on the control input, namely $d = 0$. Take the lift coefficient response C_l as the model output and also the feedback data. Therefore, the performance metric of MVC can be expressed as

$$J = E\left\{[C_l(k) - C_{lr}(k)]^2\right\}. \tag{4.8}$$

And the minimum variance self-tuning control law shown in (4.7) can be further simplified as follows:

$$\beta(k) = \frac{A(k)C_{lr}(k)}{B(k)}. \tag{4.9}$$

In this equation, $\beta(k)$ represents the deflection of the trailing-edge flap, $A(k)$ and $B(k)$ are the identified parameter matrices and $C_{lr}(k)$ signifies the target lift coefficient output, all specified at time k.

4.2.1. *Influence of different target outputs*

The ideal effect of transonic buffet control is to make the self-excited oscillation shock wave stationary, and the unstable flow eventually approaches a steady state without

https://doi.org/10.1017/jfm.2025.10755 Published online by Cambridge University Press

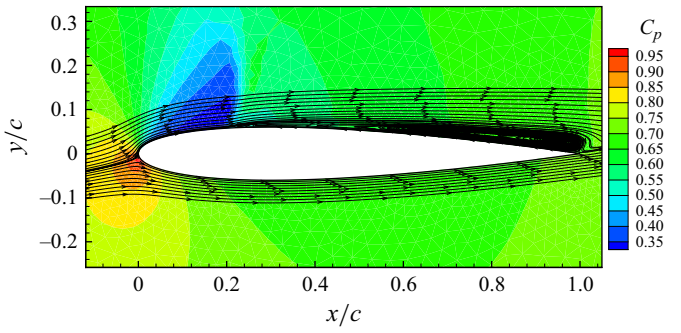


Figure 14. The pressure distribution of the unstable steady solution when $Ma = 0.70$, $\alpha = 5.5°$.

changing the incoming flow conditions and the shape of the aerofoil. This steady state strictly satisfies the boundary conditions and control equations in mathematics, that is, the unstable steady solution of the flow system. In previous research, such as the work of Ren *et al.* (2024), the unstable steady solution was used as a reference for optimal DRL control, thereby achieving complete suppression of buffet loads. Therefore, the lift coefficient corresponding to the unstable steady solution is first employed as the target output of the control system in this paper.

This article first conducts research on the control of transonic buffet over a NACA 0012 aerofoil in the state of $Ma = 0.7$ and $\alpha = 5.5°$, where the buffet phenomenon is relatively apparent. Gao *et al.* (2017) once carried out transonic buffet control research under this state, achieving complete suppression of the fluctuating loads through the linear quadratic (LQ) method. The unstable steady lift coefficient after control is $C_{l0} = 0.5529$, and the non-dimensional pressure distribution in this state is presented in figure 14.

Considering the influence of the unstable zeros of $B(z^{-1})$, this paper chooses to linearly soften the target output in order to avoid situations where the initial deflection angle of the trailing-edge flap could cause significant disturbances to the sensitive flow system or exceed the maximum deformation limits allowed by the dynamic grid method, both of which may lead to simulation failure (see Appendix B for details). Specifically, it is to introduce a softening coefficient γ to balance the weight of unstable steady solution and the last step output. The target output is constructed by the linear superposition of these two terms as follows:

$$C_{lr}(k) = (1-\gamma)C_{l0} + \gamma C_l(k-1). \tag{4.10}$$

The control effects under different softening coefficients are compared in figure 15. It can be seen that after increasing the softening coefficient, the impact caused by instantaneous deformation is reduced, and the deflection angle of the flap is within the acceptable range of the dynamic grid method. The larger the softening coefficient, the smaller the difference between the target output and the current output, and the smaller the impact of the flap actuation on the flow system when starting control. With the two typical softening coefficients depicted in figure 15, complete suppression of buffet loads can be achieved. Ultimately, the flap angle stabilises at 0°, the lift coefficient C_l settles at the unstable steady solution of 0.5529, and the torque coefficient C_m also tends to stabilise. From the analysis, it is evident that using the unstable steady solution as the target output can effectively suppress transonic buffet loads within quite a short adjustment period. However, there are still certain challenges in utilising unstable steady solutions as target outputs. Firstly, the potential significant discrepancy between the current output and the unstable steady solution may lead to an inescapable huge impact at the very beginning

https://doi.org/10.1017/jfm.2025.10755 Published online by Cambridge University Press

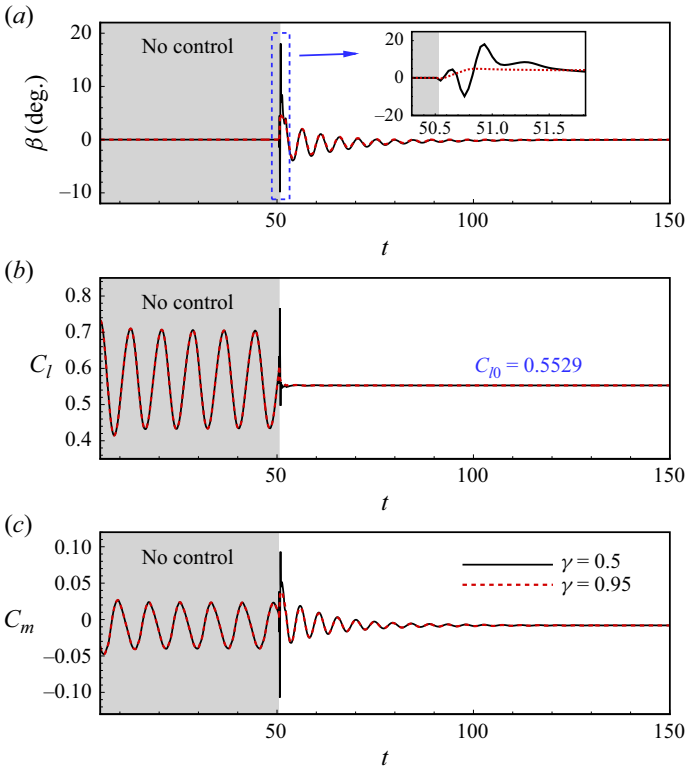


Figure 15. Comparison of control effects under different softening coefficients when $Ma = 0.70$, $\alpha = 5.5°$.

of control. Although this problem can be mitigated by limiting the controller amplitude and introducing a softening coefficient, there is still a risk of excessive adjustment time. Secondly, unstable steady solutions are not a universal target output, and, in many cases, the performance of the controlled system remains unknown, which poses significant challenges in obtaining unstable steady solutions in advance. Especially in adaptive control scenarios, where the system undergoes real-time changes under varying inflow conditions, obtaining the unstable steady solution beforehand for such continuously evolving flows is unrealistic. Therefore, it is necessary to define a more universal target output based on the response characteristics of transonic buffet.

Considering that the lift coefficient response of transonic buffet exhibits an approximate harmonic response, this paper tends to employ the mean lift coefficient response over q time steps before current time step k as the target output, as follows:

$$C_{lr}(k) = \frac{C_l(k-1) + C_l(k-2) + \cdots + C_l(k-q)}{q}. \tag{4.11}$$

This time-averaged target output changes in real time, thus overcoming the disadvantages of unstable steady solutions and facilitating the adaptive control system to efficiently achieve control objectives.

Figure 16 shows the control results under different values of forward time step q, where $q = 226$ corresponds to the number of simulation steps within a single period of transonic buffet at $Ma = 0.7$ and $\alpha = 5.5°$. It is evident that complete suppression of control objectives is achieved for varying values of q. The inevitable impact of control increases with the increase of q as the difference between current output and the target

https://doi.org/10.1017/jfm.2025.10755 Published online by Cambridge University Press

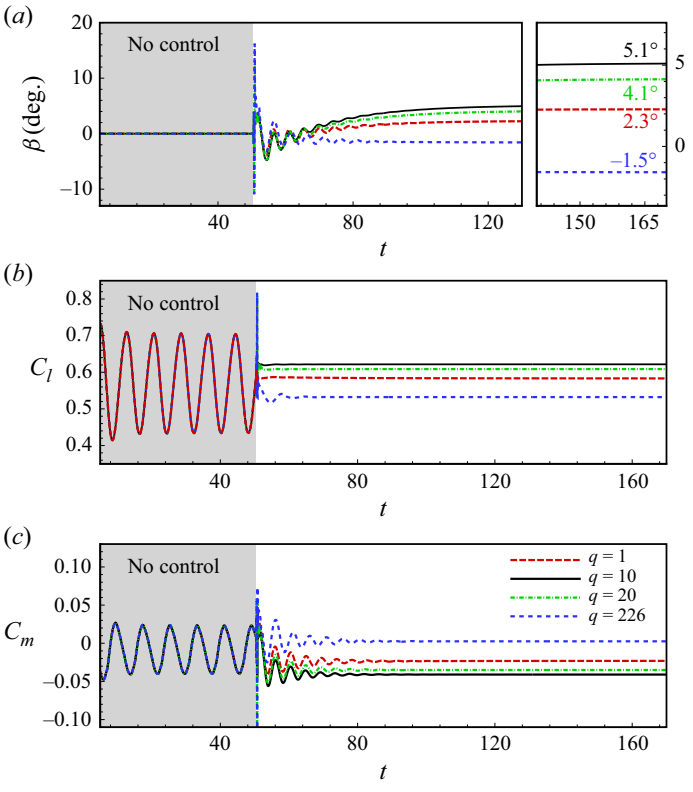


Figure 16. Buffet control effect under time-averaged target output with different q when $Ma = 0.70$, $\alpha = 5.5°$.

output increases. Nevertheless, this impact remains within the acceptable range for the dynamic grid method. In addition, the lift coefficient and flap deflection angle both tend to non-oscillatory stable states. However, these steady states differ from those observed in the unstable steady solution depicted in figure 15. To be more specific, when $q = 10$ and $q = 20$, there are stable positive flap deflection angles of 5.1° and 4.1°, respectively; when $q = 226$, the flap deflection angle converges to approximately $-1.5°$ which means that the flap ultimately deflects upward under this situation. It means that the stable deflection of the control surface adjusts the equivalent angle of attack of the aerofoil to either below the buffet-onset boundary or above the buffet-offset boundary, thereby suppressing the unsteady aerodynamic loads caused by flow separation.

This control mechanism is similar to the TED methods. However, changing the equivalent angle of attack through relevant control devices is usually undesirable during the transonic cruising state of an aircraft, as it can result in lowered mean C_l (as shown in figure 16*b*) and compromised aerodynamic efficiency. To avoid this, the final flap deflection angle should be constrained through appropriate design of the control performance metric.

4.2.2. *Validation of MVC's effectiveness*

This section further verifies the control effect of MVC at $Ma = 0.75$ and $\alpha = 3.5°$, which employs the time-averaged lift coefficient calculated by (4.11) as the target output, with $q = 20$. The control results of MVC at this state are shown in figure 17.

https://doi.org/10.1017/jfm.2025.10755 Published online by Cambridge University Press

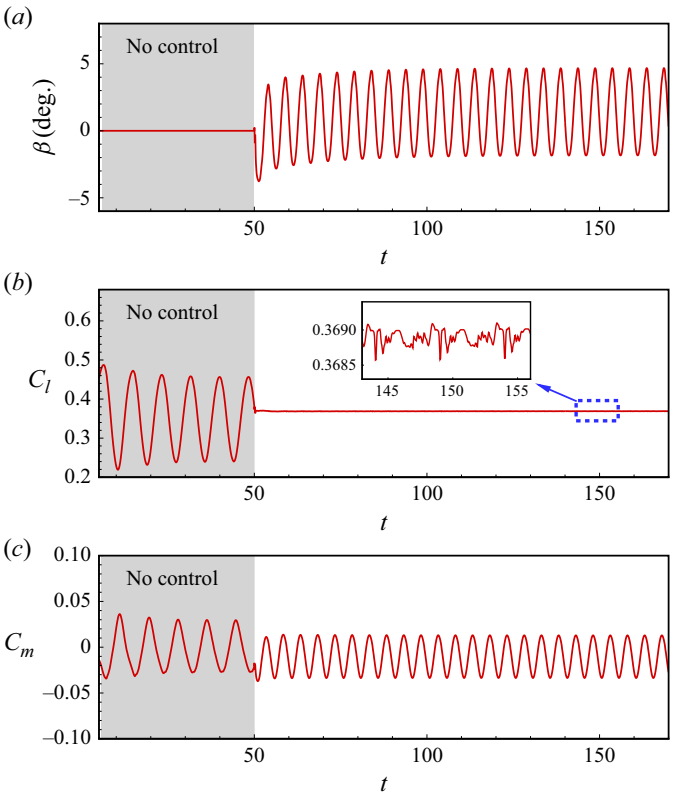


Figure 17. Control effect of MVC at $Ma = 0.75$ and $\alpha = 3.5°$.

As the figure illustrates, when control starts, the fluctuation characteristics of the lift coefficient rapidly weaken and its value ultimately converges to a nearly stable state around 0.34, which is close to the unstable steady solution $C_{l0} = 0.357$ obtained in the work of Gao *et al.* (2016). The performance metric J also rapidly decays and approaches 0. From the perspective of the responses of lift coefficient and performance metric, it can be concluded that MVC eventually achieves satisfactory suppression of buffet loads. However, despite the convergence of the lift coefficient response to a stable value, the flap continues to actuate with an amplitude of approximately 3°, rather than converging to 0° as shown in figure 16. Additionally, the shock wave and torque coefficient also exhibit continuous oscillation (with the torque integration point at 25 % chord length), indicating that while the flap oscillation controls the lift load, the shock waves in the flow field remain unstable.

Next, the mechanism behind this interesting phenomenon is further analysed. Figure 18 shows the power spectrum analysis results of the torque coefficient response before and after control. It can be seen that the dimensionless frequencies of the response before and after control are separately $f_b = 0.060$ and $f_c = 0.098$ (equal to the actuating frequency of flap). The latter frequency is 1.63 times the former one ($f_c/f_b = 1.63$), which is consistent with the optimal open-loop control frequency ratio obtained in the work of Gao *et al.* (2017) through extensive simulations.

Figure 19 further demonstrates the relationship between the flap deflection angle and the position of the shock wave after stabilising the control response. According to the definition, the downward deflection of the control surface is positive. The figure reveals

https://doi.org/10.1017/jfm.2025.10755 Published online by Cambridge University Press

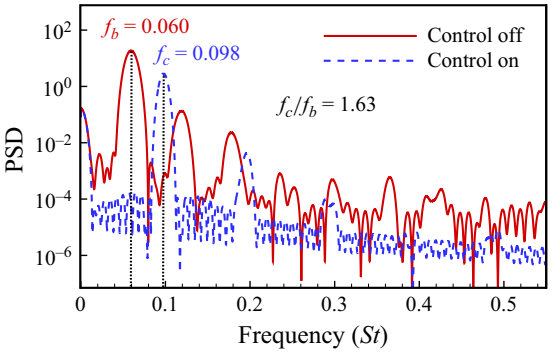


Figure 18. Power spectrum analysis results of torque coefficient response with and without MVC at $Ma = 0.75$ and $\alpha = 3.5°$. PSD-Power Spectral Density.

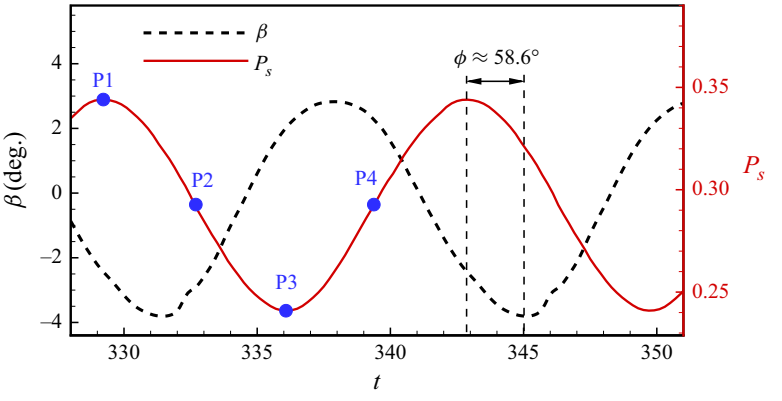


Figure 19. The relationship between shock wave oscillation and flap deflection under feedback control when $Ma = 0.75$, $\alpha = 3.5°$.

that the deflection of the control surface and the position of the shock wave both exhibit approximately harmonic response characteristics, with nearly identical response periods. Based on these response characteristics, this paper further calculates the phase difference between the shock wave oscillation response and the flap deflection, revealing a lag phase angle ϕ of approximately 58.6°. Comparing this with the delay of the lift coefficient response on flap deflection, estimated to be approximately 60° using the phase delay calculation method proposed by Gao *et al.* (2017) for subcritical states, we find that the two delay phase angles are nearly identical. In essence, given the minimal phase delay in the aerodynamic response (the aerodynamic response and shock wave oscillation response are almost synchronous) to the flap deflection, the designed closed-loop control law functions effectively as an inverse control mechanism for both shock wave oscillation and aerodynamic responses.

Figure 20 shows a comparison of pressure coefficients, flow field cloud maps and flap deflections at several typical states labelled in figure 19. When the shock wave reaches its maximum position $P_s = 0.344$, the area enclosed by the leading edge of the aerofoil and the shock wave position is relatively large. At this time, if taking the phase delay into consideration, the flap deflects precisely at the maximum upward position. The upward deflection of the control surface is equivalent to reducing the effective angle of attack of the aerofoil, and the lift coefficient caused by the flap's motion is negative, as shown in

https://doi.org/10.1017/jfm.2025.10755 Published online by Cambridge University Press

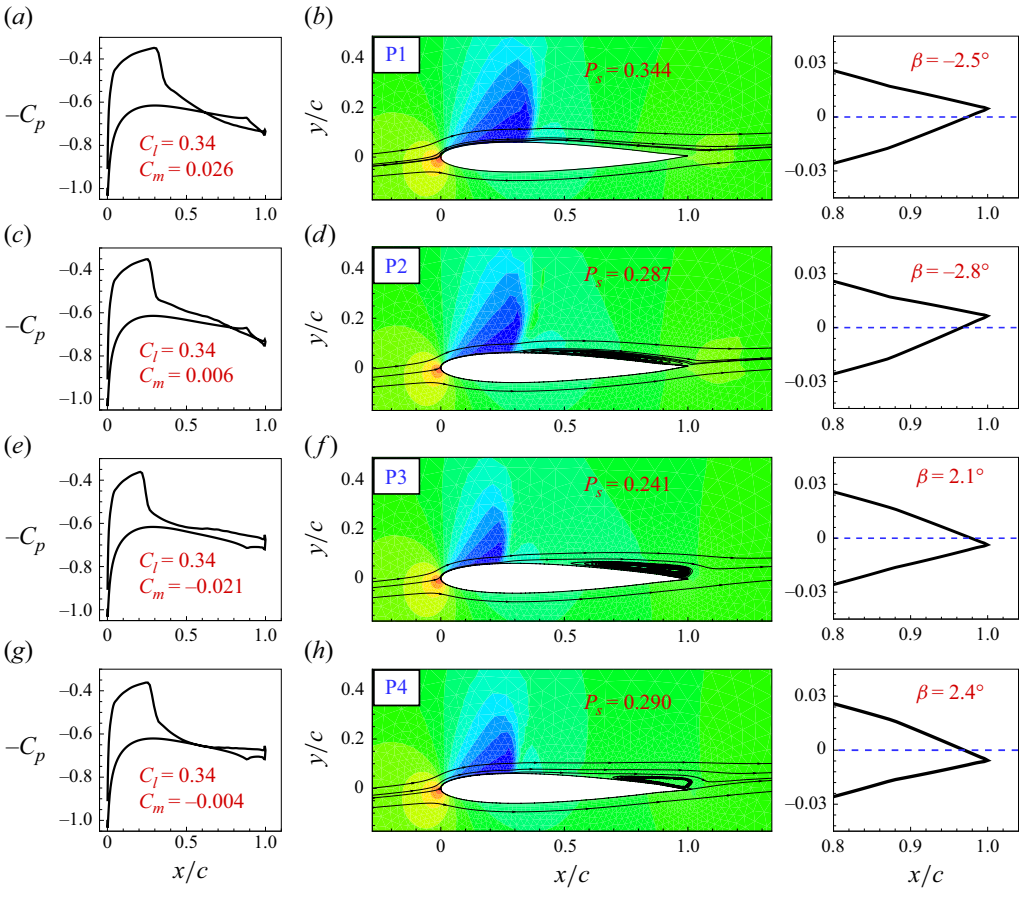


Figure 20. Comparison of pressure coefficients, flow field cloud maps and flap deflections under typical conditions after MVC at $Ma = 0.75$ and $\alpha = 3.5°$.

figure 20(*a*). Therefore, although the shock wave in this state is at the rear, the upward flap deflection guided by feedback control partially offsets the lift coefficient, resulting in a total lift coefficient of 0.34. When the shock wave reaches the forward position at $P_s = 0.241$, although the area enclosed by the leading edge of the aerofoil to the shock wave position is small, the control surface deflects precisely to its maximum downward position, which is equivalent to increasing the effective angle of attack of the aerofoil, thus increasing the lift coefficient and compensating for the loss of lift coefficient caused by the shock wave's forward movement. So the total lift coefficient remains equal to 0.34. Similarly, in other states, although the position of the shock wave changes and the lift coefficient generated by the shock wave is slightly different, feedback control can always guide the corresponding flap deflection based on the inverse control mechanism, adjust the lift coefficient, and maintain the total lift coefficient at 0.34.

From the analysis, it can be seen that the closed-loop flap control strategy guided by MVC based on the ITV-ROM achieves a similar effect to the open-loop control in the work of Gao *et al.* (2017), which further demonstrates that the actuator frequency is a crucial parameter in open-loop control. Although this control law can effectively suppress the fluctuation of the lift coefficient, the flap deflection angle still changes harmonically, and the flow field does not reach a steady state ultimately. This phenomenon can be attributed

https://doi.org/10.1017/jfm.2025.10755 Published online by Cambridge University Press

to the lack of constraints on the control input in the construction of the performance metric shown in (4.3). Therefore, when the lift coefficient approaches the target value, the flow field may not necessarily reach a steady state. If constraints are imposed on both the lift coefficient and the control input (flap deflection angle), the flow field will also reach a steady state when both the lift coefficient and flap angle approach the target value.

5. The ITV-ROM-based GPC

To overcome the aforementioned shortcomings of MVC, Clarke, Mohtadi & Tuffs (1987) proposed the GPC method, also known as multi-step predictive self-tuning control. This control algorithm builds upon the principles of online identification, output prediction, and minimum output variance control inherent in the MVC. Furthermore, it employs a rolling optimisation strategy, enabling it to simultaneously exhibit the performance characteristics of both adaptive control and predictive control. Successful applications of this method can be seen in the works of Kegerise *et al.* (2007*a*,*b*), Song *et al.* (2007) and Takahashi *et al.* (2011). This section introduces the methodology of GPC at first. And then the influence of controller parameters and validation of GPC's effectiveness are discussed in § 5.2. Besides, § 5.3 further analyses the characteristics of this flow system under control to deepen the understanding of its global instability.

5.1. *Methodology of GPC*

Consider the discrete-time system described in (4.1) and transform it into (5.1) to describe the relationship between control input increment and response output:

$$\hat{A}(z^{-1})y(k) = z^{-d}B(z^{-1})\Delta u(k), \tag{5.1}$$

where

$$\begin{cases} \hat{A}(z^{-1}) = A(z^{-1})(1-z^{-1}) = 1 + a_{1,1}z^{-1} + \cdots + a_{1,na+1}z^{-(na+1)}, \\ B(z^{-1}) = b_{1,0} + b_{1,1}z^{-1} + \cdots + b_{1,nb}z^{-nb}, \end{cases} \tag{5.2}$$

and $a_{1,0} = 1$, $a_{1,na+1} = A_{na}$; $a_{1,i} = -A_i + A_{i-1}$, $1 \leqslant i \leqslant na$; $b_{1,j} = B_{d+j}$, $0 \leqslant i \leqslant nb$.

The minimum variance output prediction model of the system at the future time $(k+N)$ can be written as:

$$\boldsymbol{Y}^* = \tilde{\boldsymbol{Y}} + \boldsymbol{G}\Delta\boldsymbol{U}, \tag{5.3}$$

where

$$\begin{cases} \boldsymbol{Y}^* = [y^*(k+d\mid k),\, y^*(k+d+1\mid k),\, \cdots,\, y^*(k+N\mid k)]^{\mathrm{T}}, \\ \tilde{\boldsymbol{Y}} = [\tilde{y}(k+d),\, \tilde{y}(k+d+1),\, \cdots,\, \tilde{y}(k+N)]^{\mathrm{T}}, \\ \boldsymbol{U} = [u(k),\, u(k+1),\, \cdots,\, u(k+N-d)]^{\mathrm{T}}, \\ \Delta u(k+i) = u(k+i) - u(k+i-1),\ i = 0,\, 1,\, \cdots,\, N-d, \\ \Delta\boldsymbol{U} = [\Delta u(k),\, \Delta u(k+1),\, \cdots,\, \Delta u(k+N-d)]^{\mathrm{T}}, \\ \boldsymbol{G} = \begin{bmatrix} b_{1,0} & 0 & \cdots & 0 \\ b_{2,0} & b_{1,0} & \cdots & 0 \\ \vdots & \vdots & \ddots & \vdots \\ b_{N-d+1,0} & b_{N-d,0} & \cdots & b_{1,0} \end{bmatrix}_{(N-d+1)\times(N-d+1)}. \end{cases} \tag{5.4}$$

https://doi.org/10.1017/jfm.2025.10755 Published online by Cambridge University Press

The predicted output $\tilde{y}(k+j)$ of step $(k+j)$ can be expressed as

$$\tilde{y}(k+j)=\sum_{i=1}^{na}a_{1,i}\tilde{y}(k+j-i)+\sum_{i=0}^{nb}b_{1,i}\Delta u(k+j-d-i|k),\ j=1,2,\cdots,N,\quad(5.5)$$

where

$$\begin{cases}\tilde{y}(k+i)=y(k+i),\ i\leqslant 0,\\ u(k+i|k)=\begin{cases}0,\ i>0\\ u(k+i),\ i\leqslant 0.\end{cases}\end{cases}\quad(5.6)$$

The elements in the control matrix $\boldsymbol{G}$ are recursively obtained from the following equation:

$$b_{j,0}=b_{1,j-1}-\sum_{i=1}^{j_1}a_{1,i}b_{j-i,0},\quad j=2,3,\cdots,N-d+1,\quad(5.7)$$

in which $j_1=\min\{j-1,na\}$. When $j-1>nb$, $b_{1,j-1}$ equals to 0.

After obtaining the predicted output at time N, the target reference output sequence $\boldsymbol{Y}_r$ can be constructed:

$$\boldsymbol{Y}_r=[y_r(k+d),\ y_r(k+d+1),\cdots,\ y_r(k+N)]^{\mathrm{T}}.\quad(5.8)$$

In control law design, the variance of the actual output over the target output and the controller characteristic weighting index are used as the control objectives, and the performance metric of GPC is defined as follows, where $\boldsymbol{\Gamma}_i=\Gamma_i\boldsymbol{I}$ $(1\leqslant i\leqslant(N-d+1))$ represent the weight matrices:

$$\begin{aligned}J&=J_1+J_2+J_3\\&=E\{(\boldsymbol{Y}-\boldsymbol{Y}_r)^{\mathrm{T}}(\boldsymbol{Y}-\boldsymbol{Y}_r)+(\boldsymbol{U}+\Delta\boldsymbol{U})^{\mathrm{T}}\boldsymbol{\Gamma}_1(\boldsymbol{U}+\Delta\boldsymbol{U})+\Delta\boldsymbol{U}^{\mathrm{T}}\boldsymbol{\Gamma}_2\Delta\boldsymbol{U}\}.\end{aligned}\quad(5.9)$$

The performance metric can be further decomposed into three components, which are $J_1=E\{(\boldsymbol{Y}-\boldsymbol{Y}_r)^{\mathrm{T}}(\boldsymbol{Y}-\boldsymbol{Y}_r)\}$ representing the constraint that ensures the outputs approach those of the target, $J_2=E\{(\boldsymbol{U}+\Delta\boldsymbol{U})^{\mathrm{T}}\boldsymbol{\Gamma}_1(\boldsymbol{U}+\Delta\boldsymbol{U})\}$ aiming to minimise the amplitude of inputs and $J_3=E\{\Delta\boldsymbol{U}^{\mathrm{T}}\boldsymbol{\Gamma}_2\Delta\boldsymbol{U}\}$ limiting the changes in inputs between two consecutive time steps to prevent huge impacts to the flow system. By minimising the performance metric as the optimisation direction, the expression for the control increment vector can be obtained as follows:

$$\Delta\boldsymbol{U}=(\boldsymbol{G}^{\mathrm{T}}\boldsymbol{G}+\boldsymbol{\Gamma}_1+\boldsymbol{\Gamma}_2)^{-1}[\boldsymbol{G}^{\mathrm{T}}(\boldsymbol{Y}_r-\tilde{\boldsymbol{Y}})-\boldsymbol{\Gamma}_1\boldsymbol{U}].\quad(5.10)$$

Therefore, the control input at time step k can be written as follows:

$$u(k)=u(k-1)+\Delta u(k),\quad(5.11)$$

The whole GPC algorithm can be concluded as Algorithm 2.

Compared with MVC, there are two typical improvements in GPC. The first is that the performance metric of GPC additionally introduces two weighted terms, J_2 and J_3, considering the input amplitude and change amount of the controller separately. This introduction can effectively overcome the disadvantage of MVC which lacks constraints on input. The second is that the control objective in GPC is not a fixed global optimisation objective, but a finite-time domain optimisation control employing a rolling optimisation strategy. Control is conducted repeatedly online, rather than offline in a single instance. At each sampling time, the control performance metric incorporates the future finite-time

https://doi.org/10.1017/jfm.2025.10755 Published online by Cambridge University Press

Algorithm 2 algorithm of GPC

Initialise: $\boldsymbol{\theta}(0)$, $\boldsymbol{P}(0)$ for RLS, N for prediction, and $\boldsymbol{\Gamma}_i$ for performance metric
Input: t_{stop} as the control stop time,
1: **for** each $k \in [1, t_{stop}]$ **do**
2: Sample current output $y(k)$ and target output $y_r(k+d)$,
3: Use RLS to estimate $\tilde{\boldsymbol{\theta}}(k)$, $\hat{A}(z^{-1})$ and $B(z^{-1})$,
4: Construct vectors $\boldsymbol{Y}^*$, $\tilde{\boldsymbol{Y}}$, $\boldsymbol{Y}_r$ and $\boldsymbol{U}$,
5: Calculate control matrix $\boldsymbol{G}$,
6: Execute $u(k)$ according to (5.11).
7: **end for**

domain which advances synchronously with the sampling time. This limited time domain optimisation objective may only yield global suboptimal solutions, but the controller can effectively track and adapt to the system's local dynamic characteristics in real time through repeated online model prediction and control. Therefore, the control system maintains effective optimality and achieves the goal of adaptive control, particularly in scenarios with time-variant incoming flow conditions.

5.2. *GPC for transonic buffet*

This section adopts the same assumptions as § 4.2. According to the framework of GPC, it is necessary to determine the target reference output sequence. Considering the difficulty in obtaining the unstable steady solution of the transonic buffet system, the average lift coefficient response over a period of time is used as the target reference output, as follows:

$$\begin{cases} \boldsymbol{Y}_r = [y_r(k),\, y_r(k+1),\, \cdots,\, y_r(k+N)]^{\mathrm{T}}, \\ y_r(k+i) = y_r(k),\, i = 0, \cdots, N, \\ y_r(k) = \dfrac{C_l(k-1) + C_l(k-2) + \cdots + C_l(k-q)}{q}. \end{cases} \tag{5.12}$$

The deflection law of the trailing-edge flap designed by GPC can be formulated as follows:

$$\begin{aligned} \beta(k) &= \beta(k-1) + \Delta\beta(k) \\ &= \beta(k-1) + [1, 0, \cdots, 0]\Delta\boldsymbol{U}, \end{aligned} \tag{5.13}$$

where $\Delta\boldsymbol{U}$ is calculated by (5.10).

5.2.1. *Influence of controller parameters*

From the design framework of GPC, the controller consists of three sets of variable parameters, namely the width N of recursive prediction, the number of forward time steps q for constructing the target output, and the weighted coefficients Γ_1 and Γ_2 in the performance metric. The influence of these parameters on the control effect is studied in this section at $Ma = 0.70$ and $\alpha = 5.5°$.

We first investigate the influence of the two weighted coefficients and other parameters are set as $N = 4$ and $q = 20$. As (5.9) shows, Γ_1 represents the weight of the actuation amplitude of flap in the performance metric, which is introduced to avoid unexpected static deflection of flap similar to those shown in figure 16. However, if Γ_1 is too large, the control adjustment time tends to increase or even fails to achieve effective suppression of the buffet loads. Similarly, Γ_2 represents the weight of the changes between two adjacent

https://doi.org/10.1017/jfm.2025.10755 Published online by Cambridge University Press

Γ_1	Flap amplitude β_{max} (deg.)	Control time $t_{control}$ (s)
0	Static flap deflection of 1.3°	
0.02	3.0	60
0.2	2.1	15
1.0	1.2	110

Table 3. The influence of Γ_1 on the quantitative indicators, when $\Gamma_2 = 1.0$.

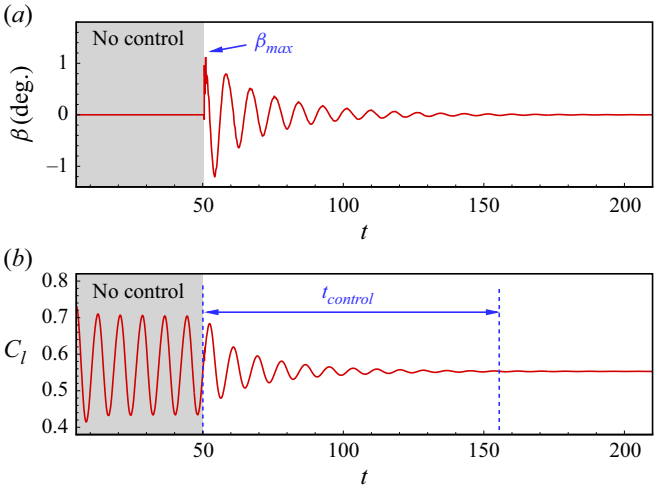


Figure 21. Schematic diagram of impact amplitude β_{max} and control time $t_{control}$.

time steps to prevent huge impacts of the control on the flow system, thereby avoiding disruption of the regular calculation of the dynamic grid method.

To illustrate the influence of the two weighted coefficients Γ_1 and Γ_2, we define two quantitative indicators: impact amplitude β_{max} and control time $t_{control}$. As figure 21 shows, the impact amplitude β_{max} refers to the maximum deflection angle of flap at the initial stage of control, and the control time $t_{control}$ represents the duration from the start of control to the end when the buffet loads are completely suppressed and the flap deflection returns to 0°. Table 3 shows the changes of these two indicators with respect to the weighting coefficients Γ_1, while Γ_2 is fixed at 1.0. The control results under typical Γ_1 are shown in figure 22. When $\Gamma_1 = 0$, although it can eliminate the pulsating buffet loads, the flap deflection angle ultimately converges to 1.3°. So under this situation, the control mechanism is still altering the effective angle of attack of the aerofoil. When $\Gamma_1 \neq 0$, not only does it achieve complete suppression of the buffet loads, but also it makes the deflection angle of the flap eventually approach 0°. From the two indicators, it is evident that when $\Gamma_1 = 0.2$, the designed control law is showing a better comprehensive performance in transonic buffet control.

Then use the same method to study the influence of Γ_2. Table 4 shows the changes of the two indicators with respect to the weighting coefficients Γ_2, with Γ_1 fixed at 0.2. When Γ_2 is too small ($\Gamma_2 = 0, 0.2$), indicating that J_3 has a relatively small weight in the performance metric, J_3 cannot effectively reduce the increment of the controller output, which results in a large deflection angle of flap and causes the failure of the dynamic grid simulation. When Γ_2 is larger than 0.5, the influence of its value on the control effect is

https://doi.org/10.1017/jfm.2025.10755 Published online by Cambridge University Press

Γ_2	Flap amplitude β_{max} (deg.)	Control time $t_{control}$ (s)
0	Unacceptable impact	
0.2	Unacceptable impact	
0.5	2.8	16
1.0	2.7	16
2.0	2.6	16
5.0	2.5	16

Table 4. The influence of Γ_2 on the quantitative indicators, when $\Gamma_1 = 0.2$.

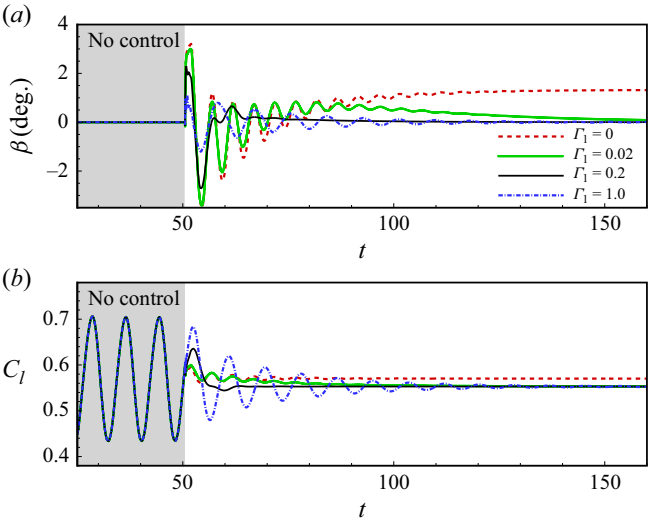


Figure 22. Control results under typical weighted coefficient Γ_1 at $Ma = 0.70$ and $\alpha = 5.5°$.

minimal, and it can always achieve complete suppression of buffet loads with little change in the control time and the initial impact. Overall, setting $\Gamma_2 = 1.0$ is the most suitable choice.

From this analysis, it can be seen that the introduction of the J_2 term in performance metric can effectively reduce the possibility of static deflection of flap at the end of control time and make the flow field converge to unstable steady solution. The term J_3 can prevent the problem of program crashes caused by large impact of the flap deflection during the initial control stage.

Then the influence of the recursive prediction width N is studied. Other parameters are determined based on previous experience ($q = 20$, $\Gamma_1 = 0.2$, $\Gamma_2 = 1.0$). Figure 23 shows the control effects under typical values of N. Generally speaking, N has little impact on control effects. So regardless of the value of N, the fluctuation of lift response is always completely suppressed with a zero flap deflection angle in the end. Therefore, for the delay free transonic buffet example studied in this paper, N is not the core parameter for GPC. From the given three sets of results, it can be observed that when N takes a large value ($N = 8$), the impact caused by the deflection of flap β_{max} at the initial stage of control is significant. When the value of N is small ($N = 1$), the aerodynamic response converges more slowly. Therefore, in subsequent studies, $N = 4$ is selected as the most suitable value.

https://doi.org/10.1017/jfm.2025.10755 Published online by Cambridge University Press

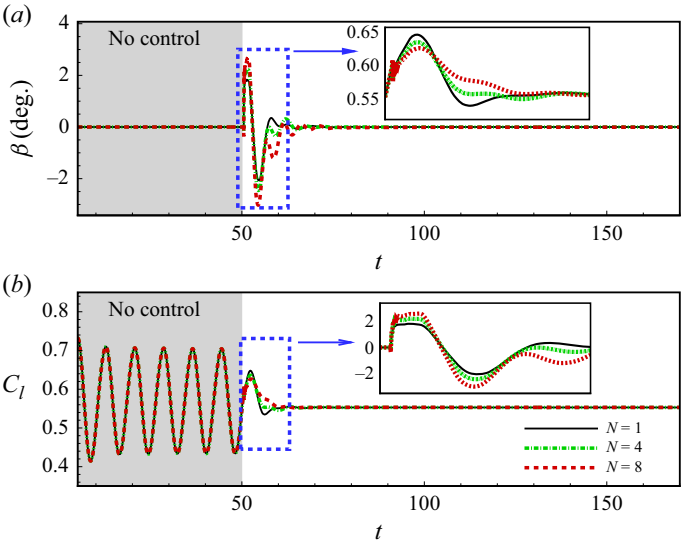


Figure 23. The influence of recursive prediction width N on control effect at $Ma = 0.70$ and $\alpha = 5.5°$.

Finally, the impact of the target output's forward time steps q is studied, where $N = 4$, $\Gamma_1 = 0.2$ and $\Gamma_2 = 1.0$. Figure 24 shows the control results under typical q values. It can be seen that when $q = 10$, 20, 226, the designed adaptive closed-loop control laws are all effective enough. From the perspective of control process, when $q = 226$, the control time $t_{control}$ is relatively long. When $q = 10$, the impact at the beginning of control is significant, which is not conducive to the stability of the system. When $q = 20$, it is possible to achieve a balance between control time $t_{control}$ and impact amplitude β_{max}.

It is noteworthy that when $q = 1$, although the deflection angle of flap eventually converges to 0°, the lift and torque coefficients are still oscillating. The amplitude and frequency of these oscillation phenomenon are basically consistent with those observed in the uncontrolled state, as shown in figure 25. This phenomenon is not unique to $q = 1$ but also occurs when $q \leqslant 3$. This indicates that when q is small, the difference between the current and target output is small, resulting in the closed-loop feedback system failing to generate effective control excitation. Consequently, it has little effective impact on the fluctuating response and load characteristics. The analysis suggests that the number of forward steps q in constructing the target output significantly affects the control effectiveness, and $q = 20$ has been identified as the most suitable value based on current studies. Therefore, $q = 20$ is selected for subsequent research.

5.2.2. *Validation of GPC's effectiveness*

Further verification of the control effect of the GPC method is conducted under the transonic buffet state when $Ma = 0.75$ and $\alpha = 3.5°$, where $N = 4$, $q = 20$, $\Gamma_1 = 0.2$ and $\Gamma_2 = 1.0$.

Figure 26 shows the control process of GPC under this state. It can be seen that as the control is turned on, both the lift and torque coefficients are quickly suppressed and gradually converge to individual stable states, and the amplitude of the flap deflection angle also gradually converges to the equilibrium position. Figure 27 shows the pressure coefficient, flow field cloud diagram and flap deflection angle after control. It can be seen

https://doi.org/10.1017/jfm.2025.10755 Published online by Cambridge University Press

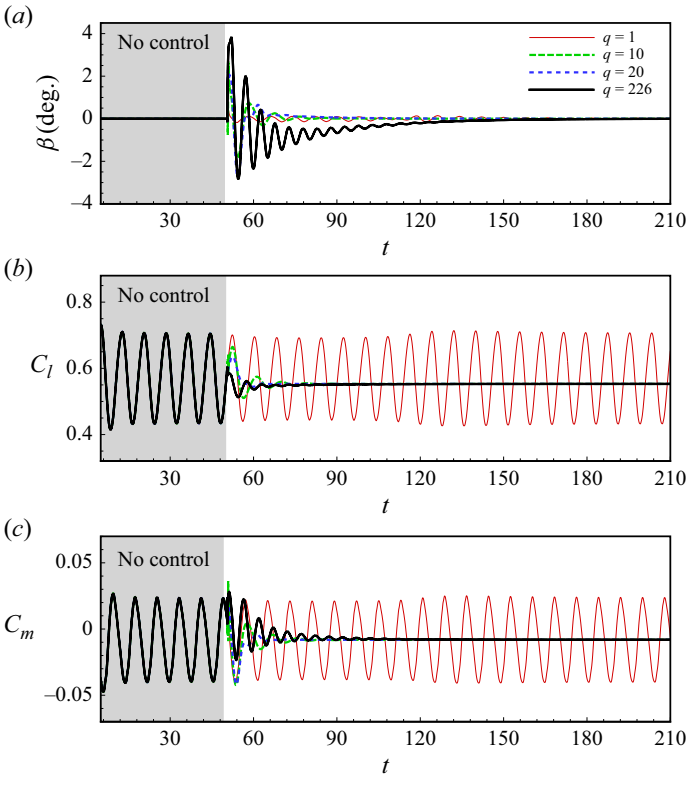


Figure 24. The influence of forward time steps q on control effect at $Ma = 0.70$ and $\alpha = 5.5°$.

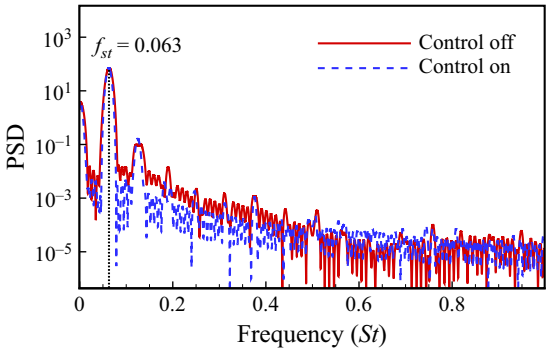


Figure 25. Power spectrum analysis results of torque coefficient response with and without GPC at $Ma = 0.70$ and $\alpha = 5.5°$. f_{st} is the natural frequency of the uncontrolled unstable flow system.

that the final flap deflection angle is 0°, without continuous oscillation or static upward deflection. Therefore, there is a fundamental difference between the control mechanism GPC here and that of changing the equivalent angle of attack revealed in § 4.2.1.

This is because in the GPC architecture, in addition to the index J_1 that characterises the output penalty, the indices J_2 and J_3 that separately suppresses the amplitude and increment of the flap deflection angle are also introduced. From the variation process of these performance metric terms during the control process shown in figure 28, it can be seen that in the initial stage of control, the overall performance metric is mainly

https://doi.org/10.1017/jfm.2025.10755 Published online by Cambridge University Press

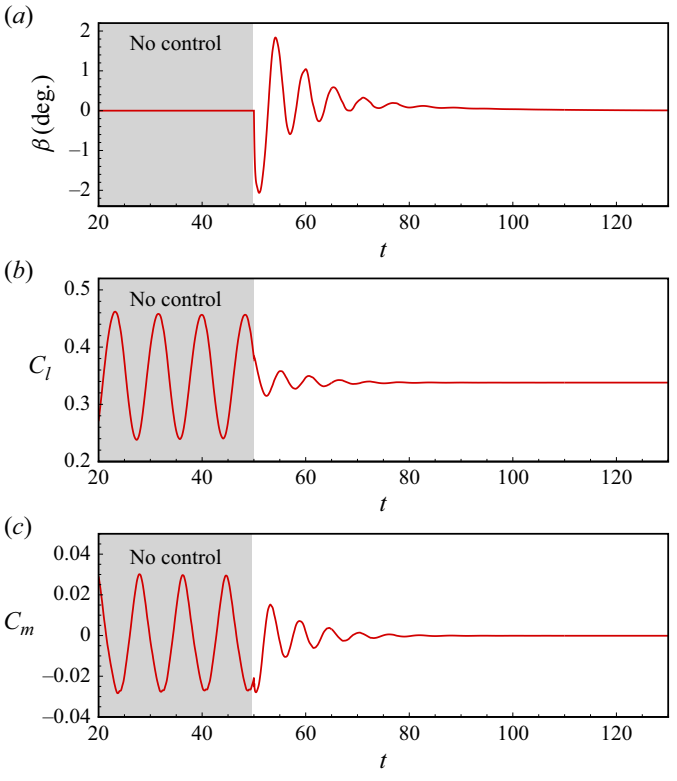


Figure 26. The control process of GPC when $Ma = 0.75$, $\alpha = 3.5°$.

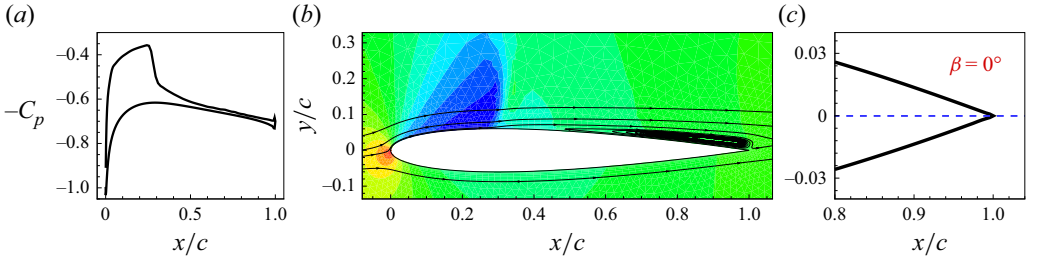


Figure 27. Pressure coefficient, flow field cloud diagram and flap deflection angle after GPC when $Ma = 0.75$, $\alpha = 3.5°$.

contributed by terms J_1 and J_3. This is because the target output is time-averaged ($q = 20$), which can effectively eliminate the excessive impact of the flap actuation and maintain the stability of the control. Therefore, the proportion of the index J_2 in the overall performance metric is relatively small. The index J_3 has the highest proportion, which further indicates that the introduction of this index plays an important role in achieving the control target.

The analysis indicates that GPC can effectively achieve satisfactory suppression of the transonic buffet with the flow field eventually converging to an unstable steady solution under different incoming flow conditions. This lays a strong foundation for adaptive control under time-variant incoming flow conditions.

https://doi.org/10.1017/jfm.2025.10755 Published online by Cambridge University Press

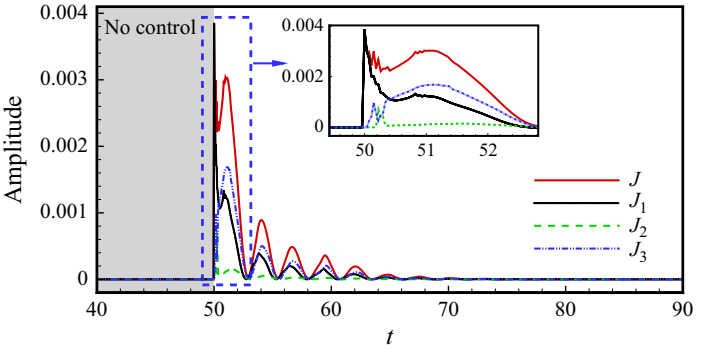


Figure 28. The variation process of the three performance metric terms when $Ma = 0.75$, $\alpha = 3.5°$.

5.3. *Characteristics of the transonic buffet flow after control*

From the existing results shown before, it can be concluded that if the control feedback loop is always activated, the flap deflection will return to 0° and the buffet phenomenon will not return even when the aerofoil is still in the buffet condition. This is because the controller employed in our study targets regulating the instability of the flow system through its pole, as shown in the derivation process of the control law guided by MVC in § 4.1. However, it is still not clear what will happen when the flap control is deactivated. Taking the best ITV-ROM-based GPC for example, this section exhibits the influence of the control switch time on the aerodynamic responses under the transonic buffet condition of $Ma = 0.70$, $\alpha = 5.5°$.

The control start time is $t = 50$, and the control off time is $t = 145$ after the flap deflection returns to 0°. As figure 29 shows, it is obvious that when the flap control is deactivated after achieving satisfactory control effect, the aerodynamic responses will re-oscillate sequentially through the linear developing stage, transition stage, and eventually converge to the nonlinear limit cycle stage. From the perspective of control, the transonic buffet flow system is further validated to be a typical global instability problem, consistent with the linear stability analysis results of Crouch *et al.* (2009). Meanwhile, it can be concluded that the feedback loop is the key element that ensures the control effectiveness, and the accuracy of the response prediction is the important foundation, indicating that the development of ITV-ROM with high accuracy is quite essential in this study.

6. Results of adaptive control under time-variant flow conditions

The effectiveness of this method in controlling the transonic buffet under given states has been verified in previous sections. However, its effectiveness under time-variant incoming flow conditions remains unknown. Therefore, in this section, further research on adaptive control under such conditions is conducted. When the incoming flow state changes, the controller must accurately predict and track the variations in flow response characteristics, and also adjust the control law of the trailing-edge flap in real time to achieve the desired control effect. Since GPC based on the ITV-ROM performed better in previous studies, it is further utilised for control research under time-variant conditions.

Table 5 briefly shows the form of the designed time-variant conditions. Active case I (AC-I) and Active case II (AC-II) demonstrate the variation of the angle of attack of the incoming flow over time when $Ma = 0.70$, the ranges of which are $\alpha = 5.0° \sim 5.5°$ and $\alpha = 4.0° \sim 6.5°$, respectively. Active case III (AC-III) illustrates a scenario where the incoming Mach number and angle of attack vary simultaneously.

https://doi.org/10.1017/jfm.2025.10755 Published online by Cambridge University Press

Case	Time-varying variables	Change modes of the variables
Active case I (AC-I)	α	Three stages: step; linear; sine
Active case II (AC-II)	α	Two stage: sine; sine
Active case III (AC-III)	Ma and α	One stage: sine

Table 5. Examples under time-variant incoming flow conditions.

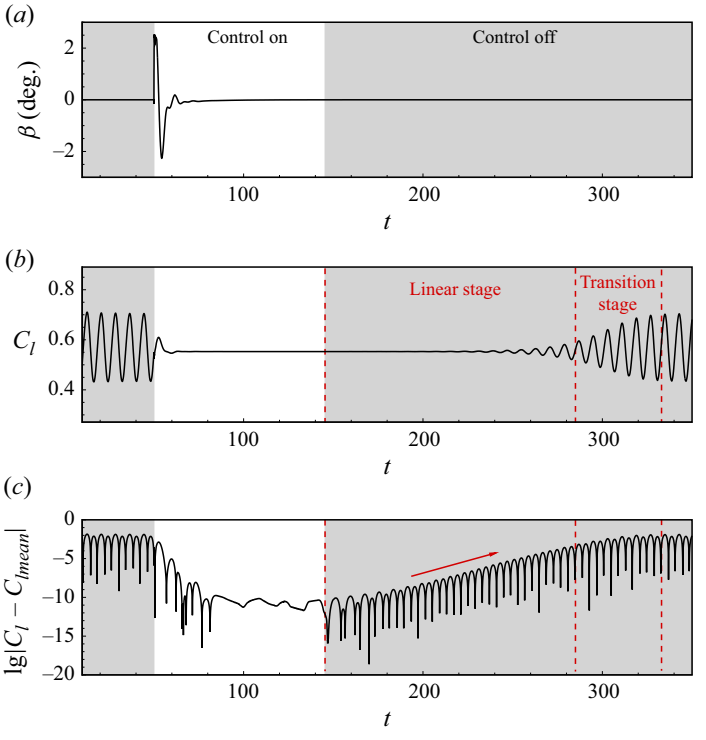


Figure 29. The lift coefficient response before and after the feedback loop turns off when $Ma = 0.70$, $\alpha = 5.5°$. C_{lmean} is the time-averaged C_l.

6.1. *AC-I*

As shown in figure 30(*a*), the variation process of the angle of attack in this example includes a step process, a linear descent process and a sine rise process. According to figure 3, it can be seen that at a Mach number of 0.7, the buffet-onset boundary is 4.8°. Therefore, during the continuous change of the angle of attack, the buffet pulsation load always exists, as shown by the black lines of figure 30. The lift and torque coefficients have different amplitude and mean values of buffet at different angles of attack.

The flap control starts at $t = 150$. The red lines in figure 30 illustrate the change trends of the lift coefficient, torque coefficient and flap deflection angle during the control process. It is evident that the control law designed using the GPC method can effectively suppress the transonic buffet under varying angles of attack. During the step change stage (region I shown in figure 30) of the angle of attack, there is a significant flap deflection angle initially due to the sudden change in the lift coefficient. Surprisingly, only approximately three cycles are required to mitigate the lift coefficient pulsation induced by the buffet

https://doi.org/10.1017/jfm.2025.10755 Published online by Cambridge University Press

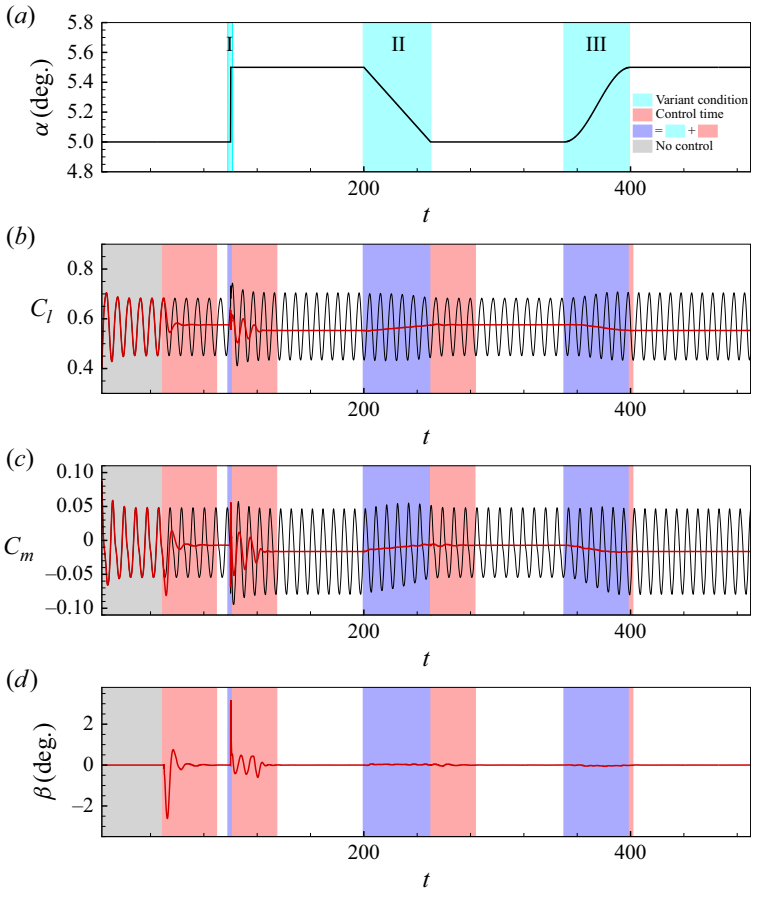


Figure 30. The change trends of the lift and torque coefficients and flap deflection angle during the control process under the condition of AC-I: $Ma = 0.70$, $\alpha = 5.0° \sim 5.5°$.

at the new angle of attack and the oscillation phenomenon after the lift coefficient's sudden drop from 0.575 to 0.553, with the flap deflection angle ultimately returning to 0°. In the linear decrease and sine rise stages (regions II and III shown in figure 30), the continuous variation of the angle of attack does not cause a sudden change in the lift coefficient. Therefore, when control is turned on, the deflection amplitude of the flap is very small, enabling a smooth transition of the flow field between different angles of attack, without significant fluctuations in the lift and torque coefficients. This control process demonstrates that the GPC method developed in this article can achieve adaptive transonic buffet control by identifying the model parameters of the complex flow system online and adjusting the controller output in response to any changes in the angle of attack of the incoming flow.

6.2. *AC-II*

The AC-II example is designed to further examine the ITV-ROM-based adaptive control effect when crossing the transonic buffet stage, as shown in figure 31(*a*). The Mach number *Ma* still remains constant at 0.70, while the angle of attack α increases from 4.0° below the buffet-onset boundary to 6.5° above the buffet-offset boundary. The buffet region is

https://doi.org/10.1017/jfm.2025.10755 Published online by Cambridge University Press

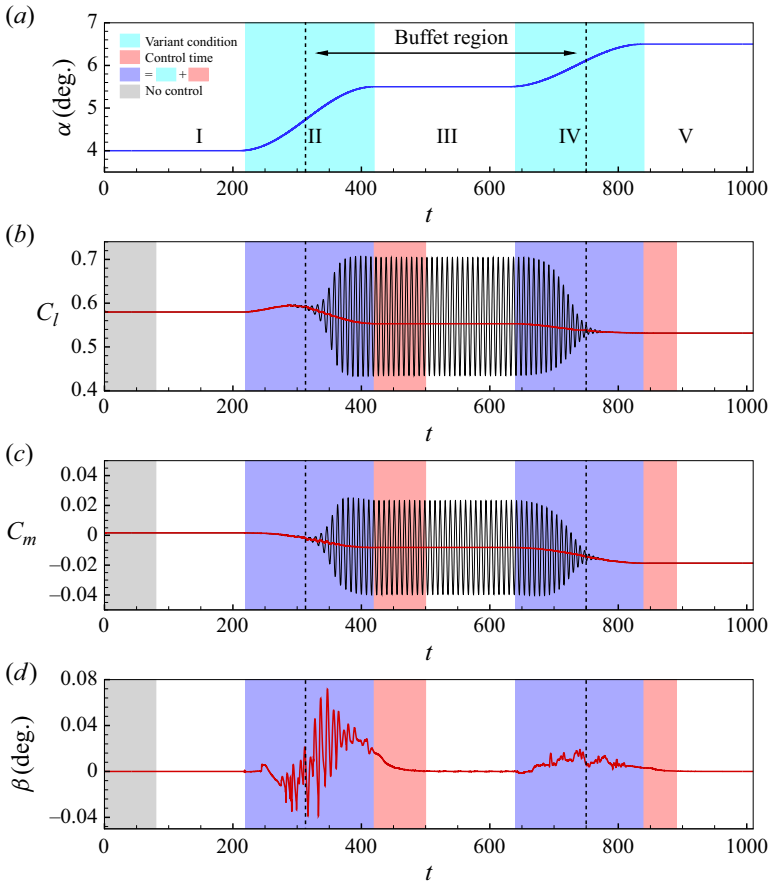


Figure 31. The change trends of the lift and torque coefficients and flap deflection angle during the control process under the condition of AC-II: $Ma = 0.70$, $\alpha = 4.0° \sim 6.5°$.

clarified by the arrow between the two black dashed lines, and the blue area shows the angle changing stage.

The flap control starts at $t = 80$. As the red lines reflecting the aerodynamic responses' history illustrate, after GPC is turned on, there is no obvious oscillation of these responses over time. It can be concluded that GPC successfully suppresses the oscillating tendency of the response as the flow system becomes unstable when the incoming flow condition changes. Figure 32 shows the frequency analyses of the lift coefficient response and the flap control law under the time-variant condition of AC-II. The dominant frequencies of them are almost the same as the intrinsic frequency of the transonic buffet flow when $Ma = 0.70$, $\alpha = 5.5°$. The smoothness of the response history is also satisfactory, indicating a great potential of ITV-ROM-based GPC in engineering applications.

Figure 33 further shows the mean pressure fields and the root-mean-squared error (RMSE) of the pressure field over typical stages shown in figure 31. As it illustrates, the edges of the shock wave are always clearer and the oscillation range of the shock wave is much smaller under the feedback control than without control during the whole condition changing stage. Therefore, it can be concluded that ITV-ROM-based GPC demonstrates excellent ability to weaken separation and stabilise the position of the shock wave, thereby ensuring the effectiveness of control during the transonic stage where the flow's unsteady characteristics are complex and highly sensitive to changes in the incoming flow state.

https://doi.org/10.1017/jfm.2025.10755 Published online by Cambridge University Press

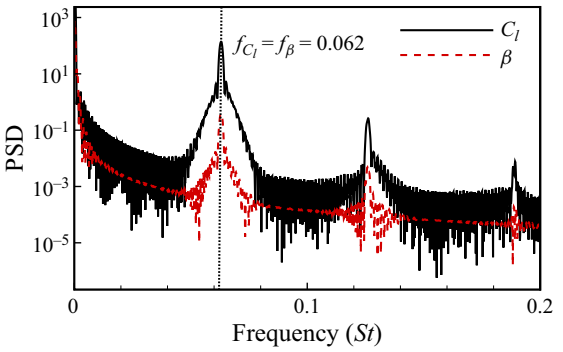


Figure 32. Frequency analyses of the lift coefficient response under control and the flap control law. f_{C_l} and f_β are the frequencies of the lift coefficient response and flap control law, respectively.

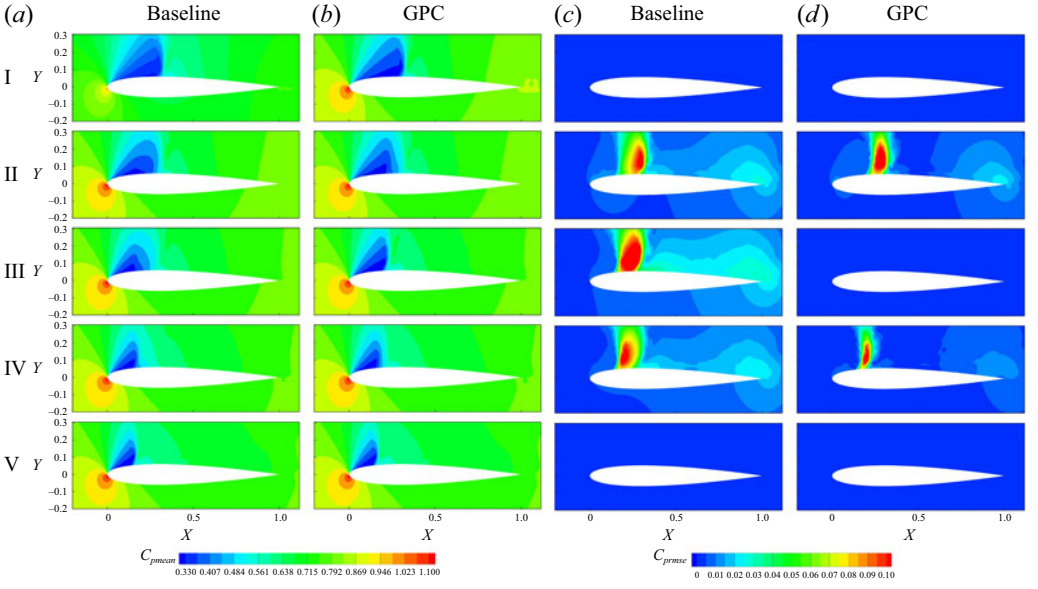


Figure 33. Mean pressure fields and RMSE of the flow fields under different stages of the condition of AC-II. C_{pmean} represents the mean pressure field, and C_{pmean} is the root-mean-squared error of the pressure field.

6.3. *AC-III*

In this example, the incoming Mach number and angle of attack change simultaneously, as shown in figure 34(*a*). The Mach number *Ma* increases from 0.70 to 0.78, and the angle of attack α decreases from 5.5° to 2.3°. Both these variants occur within the transonic buffet region shown in figure 3. Therefore, during the continuous variation of the incoming flow state, the pulsation loads caused by transonic buffet phenomenon always exist. As shown in figure 34, the lift and torque coefficients also have different fluctuating amplitudes and mean values under different incoming flow states.

The flap control starts at $t = 100$. The red lines in figure 34 also illustrate the change trends of the lift coefficient, torque coefficient and flap deflection angle during the control process. The GPC still shows a satisfactory performance in suppressing the transonic buffet with the simultaneous change of the two parameters of the incoming flow condition.

https://doi.org/10.1017/jfm.2025.10755 Published online by Cambridge University Press

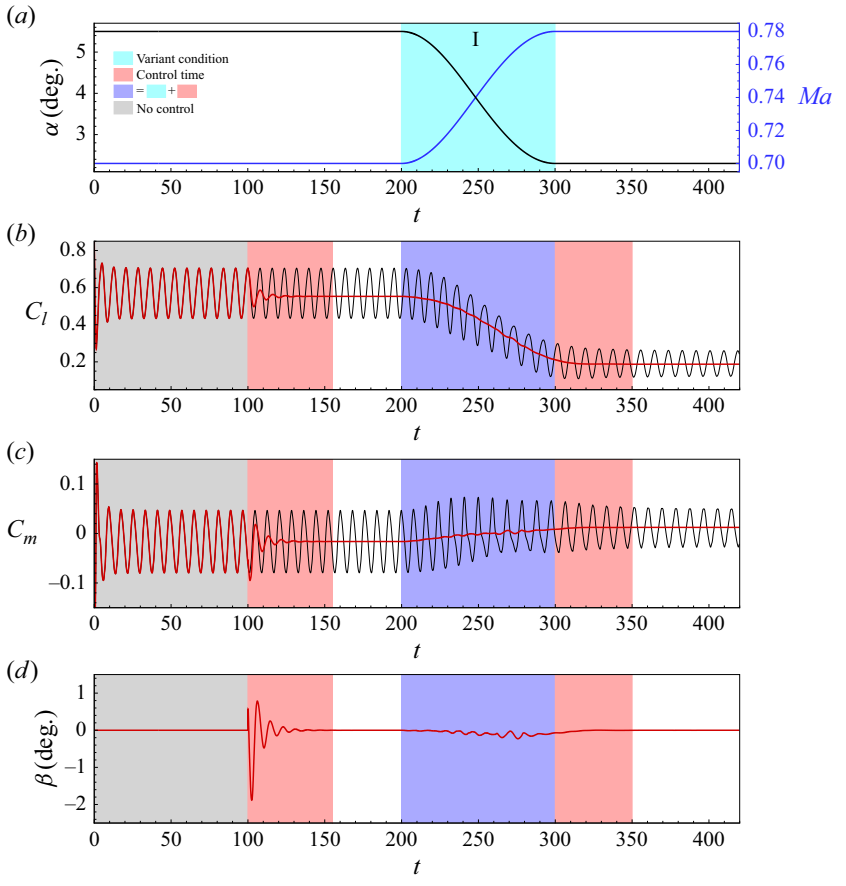


Figure 34. The change trends of the lift and torque coefficients and flap deflection angle during the control process under the condition of AC-III: $Ma = 0.70 \sim 0.78$, $\alpha = 5.5° \sim 2.3°$.

Even the flap deflection angle remains small and exhibits little fluctuation during the control process and converges automatically to 0° in the end. During this process, the lift coefficient has decreased from 0.553 to 0.187 and the torque coefficient also experiences a change from −0.016 to 0.012. The control time $t_{control}$ is quite short, occupying five cycles on average for overall suppression.

Until now, all the control processes indicate that even if the incoming flow state changes, the control law guided by the proposed method can still guide satisfactory adaptive control law design and achieve control targets without changing the effective angle of attack of the aerofoil at the end of control. The controller acts timely during the condition changing stage and the control time after the condition changing tendency ends usually lasts for less than 3 cycles before the stabilisation of the aerodynamic responses and 10 cycles before the flap completely returns to its original stage. During the actuation of the flap, the aerodynamic response of the flow system remains satisfactory in terms of smoothness and stability, especially in the example AC-II. Meanwhile, the acting frequency of the control device is almost the same as the natural frequencies of the transonic buffet at different conditions, which is approximately 18–20 Hz in reality within the maximum actuation frequency of the flight servos of large aircrafts, and the deflection amplitude of the trailing-edge flap does not exceed 3°, which is a relatively small deflection compared with those

https://doi.org/10.1017/jfm.2025.10755 Published online by Cambridge University Press

required for manoeuvre flight. Thus, it can be concluded that the range and rate of change of β is feasible under practical conditions considering the physical constraints of an actual flap.

7. Conclusions

Faced with the challenges posed by time-variant incoming flow conditions in controlling the flow systems sensitive to these external changes, this paper focuses on developing an effective adaptive control approach which combines simple self-tuning control methods with ROMs capable of tracking characteristic changes in the flow system. At first, this paper proposes an ITV-ROM method based on traditional system identification methods, enabling the flow model to reflect alternations in flow features. Subsequently, two different types of self-tuning control methods (MVC and GPC) are employed to further achieve adaptive control using the established ITV-ROM. The CFD simulation results have demonstrated the impressive effectiveness and robustness under various time-variant incoming flow conditions.

The optimal MVC requires obtaining the unstable steady solution of transonic buffet in advance to provide the target output of the control system. However, because of the lack of constraint on the control input, the deflection angle of the trailing-edge flap may not necessarily converge to zero-input state. This means that although MVC theoretically possesses the capacity to fully stabilising the self-excited oscillation of a shock wave, it often fails to maintain the original geometry of the aerofoil and results in a new steady flow with a modified shape. In contrast, GPC can overcome the disadvantage of lacking constraints on control input, achieve multi-step prediction to increase the control efficiency and reduce reliance on the unstable steady solution which is quite hard to obtain. The latter approach can effectively suppress transonic buffet and demonstrate good robustness under different time-variant incoming flow conditions.

When further analysing the control mechanism, this paper discovers that better control performance is achieved with a proper combination of time-averaged lift response and constraints on the control input into the performance metrics. Choosing the target lift coefficient over a certain time period is crucial for obtaining an appropriate time-averaged solution. Moreover, MVC can be viewed as a single-target control method, whereas GPC functions as a multi-target control method. This paper also reveals that when MVC is applied to suppressing the transonic buffet, the ultimate fluctuating frequency of the lift response aligns with the flap's deflection frequency, similar to the optimal open-loop control frequency identified by the work of Gao *et al.* (2017). And for GPC, the weight matrices are quite important in the efficiency of the designed control law. Given that the parameters are selected appropriately, this control design method can be readily applied to achieve adaptive control under time-variant incoming flow conditions, even possessing the ability to rapidly adapt to sudden changes in inflow conditions and ensuring that the flap deflection angle always converges to around 0°.

Furthermore, both the essences of the two adaptive controllers are to regulate the unstable eigenvalues of the transonic buffet flow system, thus ensuring that the shock wave buffet phenomenon will not reoccur after control ends and the deflection of flap returns to 0°. This, in turn, further validates that transonic buffet flow is a global instability system, which is consistent with the works of Crouch *et al.* (2009), Gao & Zhang (2020), Iwatani *et al.* (2023).

In conclusion, this article verifies mainly the modelling accuracy of the single-input single-output transonic buffet flow system based on the ITV-ROM method and designs adaptive controllers with single feedback signal input and single control output. However,

https://doi.org/10.1017/jfm.2025.10755 Published online by Cambridge University Press

Mesh	G1	G2	G3	G4
Aerofoil surface nodes	120	180	400	600
Mesh nodes	8568	9624	25 361	43 004
Amplitude of C_l	0.090	0.100	0.110	0.110
Amplitude of C_m	0.020	0.024	0.024	0.024
Strouhal frequency St	0.0583	0.0576	0.0573	0.0573

Table 6. Dependence of the results on different meshes differing by their spatial resolution.

the ARX model architecture is also applicable to multi-input multi-output systems, so the proposed method has the potential to be extended to a multi-feedback adaptive control based on multi-input multi-output ITV-ROMs. Meanwhile, due to the significantly lower orders of ITV-ROMs compared with the same precision TI-ROMs, it is foreseeable that as the input and output data dimensions increase, the modelling efficiency will be improved dramatically by ITV-ROMs. Moreover, this article neglected the impact of system delay, feedback delay, and noise on modelling accuracy and control design, nor did it delve into the trade-off between the model order, model accuracy and storage usage. Therefore, further research should be conducted on these aspects to apply the method to more complex flow systems and solve their corresponding modelling and control challenges.

Funding. This work was supported by the following programs: the National Natural Science Foundation of China (no. 12522211 and no. U23B6009), National Key R&D Program of China Natural Science Basic Research Program of Shaanxi (no. 2024ZC-KJXX-065), Shaanxi Innovative Research Team of Artificial Intelligence for Fluid Mechanics (2024RS-CXTD-16) and the Fundamental Research Funds for the Central Universities (no. D5000250231).

Declaration of interests. The authors report no conflict of interest.

Appendix A. Validation of numerical methods

This appendix supplements the validation of the transonic shock buffet numerical simulation methods.

A.1. *Validation of mesh and time-step convergence*

To assess the convergence in numerical computation meshes, the transonic buffet flow at $Ma = 0.7$, $Re = 3 \times 10^6$, $\alpha = 5.0°$ was computed using four different meshes: G1, G2, G3 and G4, each varying in spatial resolution. All results presented in this study are based on the G3 mesh, shown in figure 2. Detailed results are provided in table 6, showing nodal data for all meshes and the amplitude of aerodynamic forces, with nearly all values converging to within the third decimal place. Comparing G3 and G4, their results are nearly identical, yet the computational time required for G3 is less. Therefore, in this research, the G3 mesh is chosen to strike a balance between efficiency and accuracy.

For examining the temporal convergence in transonic shock buffet simulations, computations were conducted using non-dimensional computational time steps dt ranging from 0.02 to 1. Table 7 presents the aerodynamic forces and Strouhal frequencies using the G3 mesh. As the time step increases to 1.0 or higher, the CFD solver fails to capture the buffet phenomenon. Convergence of results is observed with decreasing time steps, with a non-dimensional time step no larger than 0.1 (corresponding to a physical time step of 2.94×10^{-4} s) deemed sufficient for the current simulations.

https://doi.org/10.1017/jfm.2025.10755 Published online by Cambridge University Press

Non-dimensional dt (1)	0.7	0.5	0.1	0.02
Physical dt_{real} (s)	2.06×10^{-3}	1.47×10^{-3}	2.94×10^{-4}	5.89×10^{-5}
Time-averaged C_l	0.540	0.574	0.576	0.577
Amplitude of C_l	0.090	0.108	0.110	0.110
Time-averaged C_m	0.146	0.154	0.156	0.156
Amplitude of C_m	0.012	0.024	0.024	0.024
Strouhal frequency St	0.0509	0.0567	0.0573	0.0573

Table 7. Comparison of results at different time steps.

	Turbulence models	Numerical schemes	α	ΔC_l	St
CFD	SA	ROE	3.5°	0.90–1.08	0.0684
		AUSM	3.5°	0.88–1.10	0.0668
		AUSM	3.7°	0.86–1.12	0.0700
	SST	ROE	3.5°	0.90–1.14	0.0844
		AUSM	3.5°	0.93–1.14	0.0914
		AUSM	3.7°	0.91–1.16	0.0910
Exp.		—	3.5°	—	0.0668

Table 8. The amplitude and frequency of lift coefficient in buffeting flow under different combinations of turbulence models and numerical schemes, compare with experimental results (Exp.).

A.2. *Validation of numerical simulation and experimental results*

This subsection provides a more detailed validation of numerical simulations and experimental results. Jacquin *et al.* (2009) employed an OAT15A supercritical aerofoil as an experimental model at $Ma = 0.73$, $Re = 3 \times 10^6$, $\alpha = 3.5°$, yielding extensive experimental data, particularly on buffet loads. Consequently, the simulation results of this aerofoil are applied to assess the CFD solver's accuracy in predicting buffet loads' efficiency.

Firstly, we conduct a sensitivity study of the turbulence model and numerical schemes. The far-field boundary is located 30 chord lengths away, with the first cell height of the boundary layer set at $5 \times 10^{-6}c$, and a non-dimensional wall distance of $y^+ \sim 1$. The mesh comprises 37 145 cells, and the physical time step for unsteady calculations is 2×10^{-4} s. Table 8 compares the amplitude and frequency of the buffet lift coefficient response under different combinations of turbulence models and numerical schemes, with calculation conditions set to those of the work of Jacquin *et al.* (2009). The comparison reveals that the turbulence model significantly influences the calculation results, whereas the impact of numerical schemes is relatively minor. The Shear-Stress Transport (SST) $k-\omega$ model predicts higher buffet loads and frequencies, consistent with findings in the literature. Compared with experimental results, the buffet frequency calculated using the SA turbulence model better matches the experimental data. Therefore, for this aerofoil buffet case, we employ the S-A turbulence model and AUSM spatial discretisation scheme in subsequent calculations.

Figure 35 shows the root-mean-square (RMS) values of pressure fluctuations on the upper surface of the profile, normalised by the free-stream dynamic pressure Q_0. Wall pressure fluctuations arise due to unsteady separated flow, with peaks associated with shock motion. In the present calculation, the predicted peak at $\alpha = 3.5°$ is slightly lower than the experimental one, whereas the calculated peak at $\alpha = 3.7°$ indicates better

https://doi.org/10.1017/jfm.2025.10755 Published online by Cambridge University Press

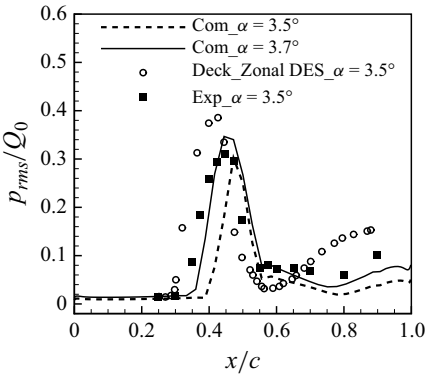


Figure 35. Influence of the incidence on the chord wise distribution of the surface pressure RMS.

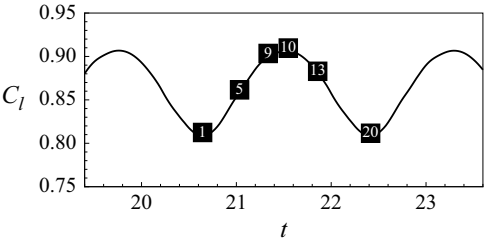


Figure 36. Schematic map of phases in one period of the shock motion.

agreement. The result simulated by Deck (2005) using Zonal-DES at $\alpha = 3.5°$ shows a higher peak. That is, loads predicted by the SA turbulence model are slightly smaller than those of the experiment. In the experiment of Jacquin *et al.* (2009), the model had a blunt trailing edge, whereas it was sharp in Deck's calculation (Deck 2005). In current simulations, both models are adopted and they share nearly consistent results. Results provided in this paper are based on the sharp model.

Velocity phase average profiles measured at 60 % chord are presented in the study of Jacquin *et al.* (2009). These profiles show that buffet leads to the periodic separation of the boundary layer and the periodic shock motion. A schematic map of the phases is shown in figure 36. Phase 1 is when the shock is in the upstream location. Figure 37 displays the velocity contours and the velocity profiles at different phases in the upper-surface location of $x/c = 0.6$, where y_s is the coordinate of the upper surface. In those computations, the boundary layer is attached at phase 5 (figure 37*b*), and the separation occurs at phase 9 (figure 37*c*). In the given four phases, velocity profiles of experiments agree well with those of calculations.

Appendix B. Influence of huge control impact

Figure 38 demonstrates the control effect when an unstable steady solution is directly set as the target output, with the control activated around $t = 50.5$. It is observable that, owing to the absence of necessary constraints on the controller output amplitude in the performance metric, a considerable impact occurs at the onset of control. Specifically, the flap deflects upwards to around 20°, and the lift coefficient surpasses twice the amplitude of the buffet load. Under such significant flap deflection, the deformation capacity of the dynamic mesh method is exceeded, resulting in the failure of the computational simulation.

https://doi.org/10.1017/jfm.2025.10755 Published online by Cambridge University Press

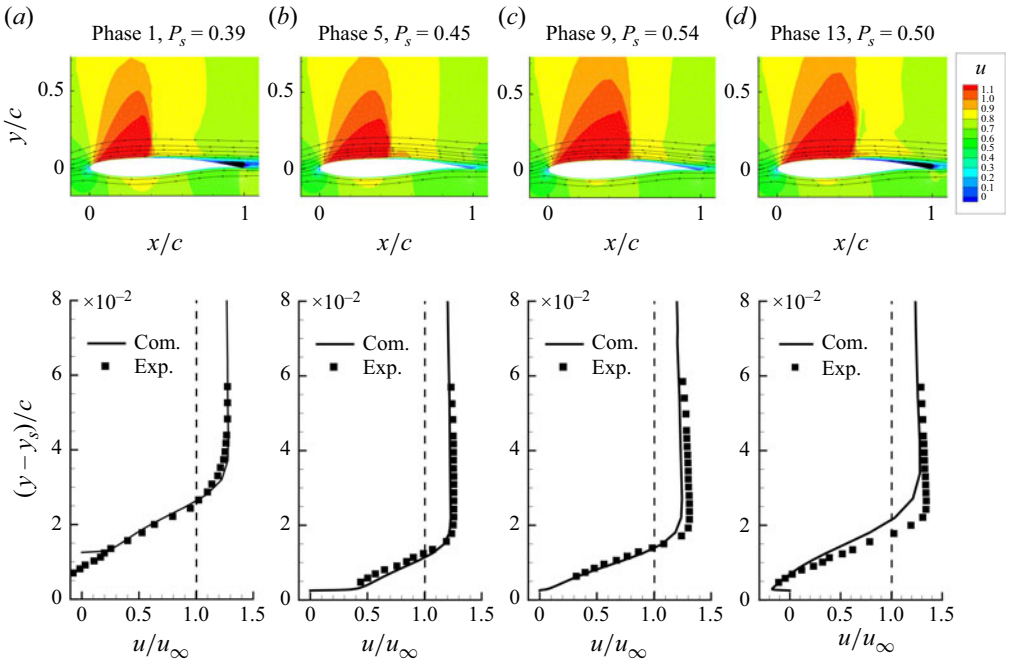


Figure 37. Non-dimensional velocity profiles of four phases in one period at $x/c = 0.6$, $Ma = 0.73$, $Re = 3 \times 10^6$, $\alpha = 3.7°$.

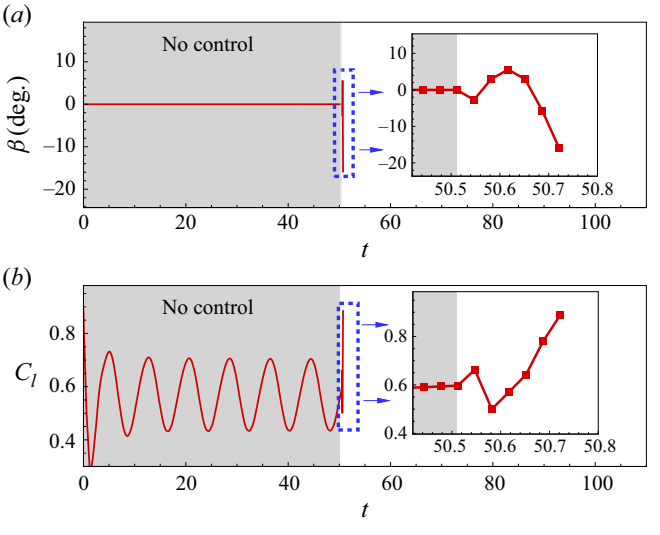


Figure 38. Control effect with unstable steady solution as the target output.

From the control performance metric in (4.8), it can be seen that the huge impact of the control system is attributed primarily to a significant difference between the system's output at the start of control and the target output. Technically, there exist various methods to mitigate this difference and, consequently, reduce the impact on the flow system. These include limiting the amplitude of the flap deflection angle (often used in experiments),

https://doi.org/10.1017/jfm.2025.10755 Published online by Cambridge University Press

selecting the optimal time to initiate control when the difference from the target output is minimal, and implementing linear softening treatment on the target output (a technique often employed in simulations).

References

Brunton, S.L. & Noack, B.R. 2015 Closed-loop turbulence control: progress and challenges. *Appl. Mech. Rev.* **67** (5), 050801.

Carini, M., Pralits, J.O. & Luchini, P. 2015 Feedback control of vortex shedding using a full-order optimal compensator. *J. Fluid. Struct.* **53**, 15–25.

Caruana, D., Mignosi, A., Corrège, M., Le Pourhiet, A. & Rodde, A.M. 2005 Buffet and buffeting control in transonic flow. *Aerosp. Sci. Technol.* **9** (7), 605–616.

Choi, H., Jeon, W.-P. & Kim, J. 2008 Control of flow over a bluff body. *Annu. Rev. Fluid Mech.* **40**, 113–139.

Clarke, D.W., Mohtadi, C. & Tuffs, P.S. 1987 Generalized predictive control–Part I. The basic algorithm. *Automatica* **23** (2), 137–148.

Couplet, M., Basdevant, C. & Sagaut, P. 2005 Calibrated reduced-order POD-Galerkin system for fluid flow modelling. *J. Comput. Phys.* **207** (1), 192–220.

Crouch, J.D., Garbaruk, A., Magidov, D. & Travin, A. 2009 Origin of transonic buffet on aerofoils. *J. Fluid Mech.* **628**, 357–369.

Dadfar, R., Hanifi, A. & Henningson, D.S. 2018 Control of instabilities in an unswept wing boundary layer. *AIAA J.* **56** (5), 1750–1759.

Dandois, J., Lepage, A., Dor, J.-B., Molton, P., Ternoy, F., Geeraert, A., Brunet, V. & Coustols, É. 2014 Open and closed-loop control of transonic buffet on 3D turbulent wings using fluidic devices. *Comptes Rendus. Mécanique* **342** (6–7), 425–436.

Deck, S. 2005 Numerical simulation of transonic buffet over a supercritical airfoil. *AIAA J.* **43** (7), 1556–1566.

Degregori, E. & Kim, J.W. 2021 Mitigation of transonic shock buffet on a supercritical airfoil through wavy leading edges. *Phys. Fluids* **33** (2), 026104.

Doerffer, P., Hirsch, C., Dussauge, J.-P., Babinsky, H. & Barakos, G.N. 2010 *Unsteady Effects of Shock Wave Induced Separation*. vol. 114. Springer Science & Business Media.

Dou, Z., Gao, C. & Zhang, W. 2024 Dynamic characteristic of transonic aeroelasticity affected by fluid mode in pre-buffet flow. *J. Fluid Mech.* **999**, A24.

Fabbiane, N., Semeraro, O., Bagheri, S. & Henningson, D.S. 2014 Adaptive and model-based control theory applied to convectively unstable flows. *Appl. Mech. Rev.* **66** (6), 060801.

Fabbiane, N., Simon, B., Fischer, F., Grundmann, S., Bagheri, S. & Henningson, D.S. 2015 On the role of adaptivity for robust laminar flow control. *J. Fluid Mech.* **767**, R1.

Friedewald, D. 2023 Large-amplitude gusts on the nasa common research model. *J. Aircraft* **60** (6), 1901–1916.

Galea, S., Henderson, D., Moses, R., Zimcik, D., White, E. & Ryall, T. 2003 Next generation active buffet suppression system. In *AIAA International Air and Space Symposium and Exposition: The Next 100 Years*, pp. 2905.

Gao, C., Ma, R., Ren, K., Yuan, H. & Zhang, W. 2025*a* Optimal position and angle of jet control for transonic shock buffet with resolvent analysis. *AIAA J.* **63** (8), 3415–3433.

Gao, C., Yang, X., Ren, K. & Zhang, W. 2025*b* Open-loop linear modeling method for unstable flow utilizing built-in data-driven feedback controllers. *Phys. Rev. Fluids* **10** (3), 033902.

Gao, C. & Zhang, W. 2020 Transonic aeroelasticity: a new perspective from the fluid mode. *Prog. Aerosp. Sci.* **113**, 100596.

Gao, C., Zhang, W., Kou, J., Liu, Y. & Ye, Z. 2017 Active control of transonic buffet flow. *J. Fluid Mech.* **824**, 312–351.

Gao, C., Zhang, W. & Ye, Z. 2016 Numerical study on closed-loop control of transonic buffet suppression by trailing edge flap. *Comput. Fluids* **132**, 32–45.

Geoghegan, J.A., Giannelis, N.F. & Vio, G.A. 2020 A numerical investigation of the geometric parametrisation of shock control bumps for transonic shock oscillation control. *Fluids* **5** (2), 46.

Hasheminejad, S.M., Rabiee, A.H., Jarrahi, M. & Markazi, A.H.D. 2014 Active vortex-induced vibration control of a circular cylinder at low reynolds numbers using an adaptive fuzzy sliding mode controller. *J. Fluid. Struct.* **50**, 49–65.

Herrmann, B., Baddoo, P.J., Dawson, S.T.M., Semaan, R., Brunton, S.L. & McKeon, B.J. 2023 Interpolatory input and output projections for flow control. *J. Fluid Mech.* **971**, A27.

Humphreys, M.D. 1951 *Pressure Pulsations On Rigid Airfoils at Transonic Speeds*. NACA.

https://doi.org/10.1017/jfm.2025.10755 Published online by Cambridge University Press

IWATANI, Y., ASADA, H., YEH, C.-A., TAIRA, K. & KAWAI, S. 2023 Identifying the self-sustaining mechanisms of transonic airfoil buffet with resolvent analysis. *AIAA J.* **61** (6), 2400–2411.

JACQUIN, L., MOLTON, P., DECK, S., MAURY, B. & SOULEVANT, D. 2009 Experimental study of shock oscillation over a transonic supercritical profile. *AIAA J.* **47** (9), 1985–1994.

JUSSIAU, W., LECLERCQ, C., DEMOURANT, F. & APKARIAN, P. 2022 Learning linear feedback controllers for suppressing the vortex-shedding flow past a cylinder. *IEEE Control Syst. Lett.* **6**, 3212–3217.

KEGERISE, M.A., CABELL, R.H. & CATTAFESTA, L.N.III 2007*a* Real-time feedback control of flow-induced cavity tones—Part 1: Fixed-gain control. *J. Sound Vib.* **307** (3–5), 906–923.

KEGERISE, M.A., CABELL, R.H. & CATTAFESTA, L.N.III 2007*b* Real-time feedback control of flow-induced cavity tones—part 2: adaptive control. *J. Sound Vib.* **307** (3–5), 924–940.

KIM, J. & BEWLEY, T.R. 2007 A linear systems approach to flow control. *Annu. Rev. Fluid Mech.* **39**, 383–417.

KIM, T., HONG, M., BHATIA, K.G. & SENGUPTA, G. 2005 Aeroelastic model reduction for affordable computational fluid dynamics-based flutter analysis. *AIAA J.* **43** (12), 2487–2495.

KOJIMA, Y., YEH, C.-A., TAIRA, K. & KAMEDA, M. 2020 Resolvent analysis on the origin of two-dimensional transonic buffet. *J. Fluid Mech.* **885**, R1.

KUZ'MIN, A. 2009 Bifurcations and buffet of transonic flow past flattened surfaces. *Comput. Fluids* **38** (7), 1369–1374.

KWON, J.R. & VEPA, R. 2023 Feedback control of limit cycle oscillations and transonic buzz, using the nonlinear transonic small disturbance aerodynamics. *J. Vib. Control* **29** (3–4), 772–783.

LECLERCQ, C., DEMOURANT, F., POUSSOT-VASSAL, C. & SIPP, D. 2019 Linear iterative method for closed-loop control of quasiperiodic flows. *J. Fluid Mech.* **868**, 26–65.

LECLERCQ, C. & SIPP, D. 2023 Mean resolvent operator of a statistically steady flow. *J. Fluid Mech.* **968**, A13.

LEE, B.H.K. 1990 Oscillatory shock motion caused by transonic shock boundary-layer interaction. *AIAA J.* **28** (5), 942–944.

LI, S., LI, W. & NOACK, B.R. 2022 Machine-learned control-oriented flow estimation for multi-actuator multi-sensor systems exemplified for the fluidic pinball. *J. Fluid Mech.* **952**, A36.

LI, X., ZHANG, W. & GAO, C. 2018 Proximity-interference wake-induced vibration at subcritical re: mechanism analysis using a linear dynamic model. *Phys. Fluids* **30** (3), 033606.

LIN, C.-T., TSAI, M.-L. & TSAI, H.-C. 2023 Flow control of a plunging cylinder based on resolvent analysis. *J. Fluid Mech.* **967**, A41.

MA, R., GAO, C., REN, K., YUAN, H. & ZHANG, W. 2024 Suppression of oscillatory fluid forces in cylinder wake: optimal jet control position designed through resolvent analysis. *Phys. Fluids* **36** (7), 073622.

MA, R., GAO, C. & ZHANG, W. 2025 Dependency of optimal jet control position on Reynolds-Number in cylinder flow via resolvent analysis. *Phys. Fluids* **37** (9), 093615.

MACEDA, G.Y.C., VARON, E., LUSSEYRAN, F. & NOACK, B.R. 2023 Stabilization of a multi-frequency open cavity flow with gradient-enriched machine learning control. *J. Fluid Mech.* **955**, A20.

MAYER, R., LUTZ, T., KRÄMER, E. & DANDOIS, J. 2019 Control of transonic buffet by shock control bumps on wing-body configuration. *J. Aircr.* **56** (2), 556–568.

MOLTON, P., DANDOIS, J., LEPAGE, A., BRUNET, V. & BUR, R. 2013 Control of buffet phenomenon on a transonic swept wing. *AIAA J.* **51** (4), 761–772.

NIBOUREL, P., LECLERCQ, C., DEMOURANT, F., GARNIER, E. & SIPP, D. 2023 Reactive control of second mack mode in a supersonic boundary layer with free-stream velocity/density variations. *J. Fluid Mech.* **954**, A20.

NIBOUREL, P., LECLERCQ, C., DEMOURANT, F., GARNIER, E. & SIPP, D. 2024 Extending closed-loop control of two-dimensional supersonic boundary-layer instabilities beyond a single operating point. *AIAA J.* **62** (3), 896–914.

PANG, Z. & CUI, H. 2013 *System Identification and Adaptive Control: MATLAB Simulation (Revision)*. Beihang University Press.

PARIS, R., BENEDDINE, S. & DANDOIS, J. 2023 Reinforcement-learning-based actuator selection method for active flow control. *J. Fluid Mech.* **955**, A8.

PARK, J. & CHOI, H. 2020 Machine-learning-based feedback control for drag reduction in a turbulent channel flow. *J. Fluid Mech.* **904**, A24.

PAWAR, S., AHMED, S.E., SAN, O. & RASHEED, A. 2020 An evolve-then-correct reduced order model for hidden fluid dynamics. *Mathematics* **8** (4), 570.

PENG, J., CHEN, S., AUBRY, N., CHEN, Z. & WU, W. 2020 Time-variant prediction of flow over an airfoil using deep neural network. *Phys. Fluids* **32** (12), 123602.

PETROCCHI, A., MAURIELLO, M. & BARAKOS, G. 2023 Transonic buffet alleviation via virtual control surfaces. *Aerosp. Sci. Technol.* **140**, 108478.

https://doi.org/10.1017/jfm.2025.10755 Published online by Cambridge University Press

POULAIN, A., CONTENT, C., RIGAS, G., GARNIER, E. & SIPP, D. 2024 Adjoint-based linear sensitivity of a supersonic boundary layer to steady wall blowing–suction/heating–cooling. *J. Fluid Mech.* **978**, A16.
REN, K., CHEN, Y., GAO, C. & ZHANG, W. 2020 Adaptive control of transonic buffet flows over an airfoil. *Phys. Fluids* **32** (9), 096106.
REN, K., GAO, C., XIONG, N. & ZHANG, W. 2024 Adaptive control of transonic buffet and buffeting flow with deep reinforcement learning. *Phys. Fluids* **36** (1), 016143.
REN, K., GAO, C., ZHOU, F. & ZHANG, W. 2022 Transonic buffet active control with local smart skin. *Actuators* **11** (6), 155.
ROWLEY, C.W. 2005 Model reduction for fluids, using balanced proper orthogonal decomposition. *Intl J. Bifurcat. Chaos* **15** (03), 997–1013.
SARTOR, F., METTOT, C. & SIPP, D. 2015 Stability, receptivity, and sensitivity analyses of buffeting transonic flow over a profile. *AIAA J.* **53** (7), 1980–1993.
SCHMID, P.J. 2010 Dynamic mode decomposition of numerical and experimental data. *J. Fluid Mech.* **656**, 5–28.
SEMERARO, O. & PRALITS, J.O. 2018 Full-order optimal compensators for flow control: the multiple inputs case. *Theor. Comput. Fluid Dyn.* **32**, 285–305.
SHI, X., GAO, C., LIU, K. & ZHANG, W. 2025 Transonic aeroelastic stability analysis of launch vehicles using reduced-order model. *Aerosp. Sci. Technol.* **168**, 110884.
SILVA, W. 2005 Identification of nonlinear aeroelastic systems based on the volterra theory: progress and opportunities. *Nonlinear Dyn.* **39**, 25–62.
SIPP, D., MARQUET, O., MELIGA, P. & BARBAGALLO, A. 2010 Dynamics and control of global instabilities in open-flows: a linearized approach. *Appl. Mech. Rev.* **63** (3), 030801.
SIPP, D. & SCHMID, P.J. 2016 Linear closed-loop control of fluid instabilities and noise-induced perturbations: a review of approaches and tools. *Appl. Mech. Rev.* **68** (2), 020801.
SONG, Q., TIAN, Y. & CATTAFESTA, L. 2007 Mimo feedback control of flow separation. In *45th AIAA Aerospace Sciences Meeting and Exhibit*, pp. 109.
STRINGER, R.M., ZANG, J. & HILLIS, A.J. 2014 Unsteady rans computations of flow around a circular cylinder for a wide range of Reynolds numbers. *Ocean Engng* **87**, 1–9.
TAKAHASHI, H., LIU, F., PALAVICCINI, M., OYARZUN, M., GRIFFIN, J., UKEILEY, L. & CATTAFESTA, L. 2011 Experimental study of adaptive control of high-speed flow-induced cavity oscillations. *J. Fluid Sci. Technol.* **6** (5), 701–716.
TIAN, Y., LI, Z. & PEIQING, L. 2018 Upper trailing-edge flap for transonic buffet control. *J. Aircraft* **55** (1), 382–389.
TIAN, Y., SONG, Q. & CATTAFESTA, L. 2006 Adaptive feedback control of flow separation. In *3rd AIAA Flow Control Conference*, pp. 3016.
TIJDEMAN, H. 1977 Investigations of the transonic flow around oscillating airfoils. NLR-TR 77090 U.
TITCHENER, N. & BABINSKY, H. 2015 A review of the use of vortex generators for mitigating shock-induced separation. *Shock Waves* **25**, 473–494.
TOL, H.J., KOTSONIS, M. & DE VISSER, C.C. 2019 Pressure output feedback control of Tollmien–schlichting waves in Falkner–Skan boundary layers. *AIAA J.* **57** (4), 1538–1551.
TOL, H.J., KOTSONIS, M., DE VISSER, C.C. & BAMIEH, B. 2017 Localised estimation and control of linear instabilities in two-dimensional wall-bounded shear flows. *J. Fluid Mech.* **824**, 818–865.
WANG, C., TANG, H., YU, S. & DUAN, F. 2017 Control of vortex-induced vibration using a pair of synthetic jets: influence of active lock-on. *Phys. Fluids* **29** (8), 083602.
WANG, X., DENG, N., MACEDA, C., GUY, Y. & NOACK, B.R. 2023*a* Cluster-based control for net drag reduction of the fluidic pinball. *Phys. Fluids* **35** (2), 023601.
WANG, Z., FAN, D., JIANG, X., TRIANTAFYLLOU, M.S. & KARNIADAKIS, G.E. 2023*b* Deep reinforcement transfer learning of active control for bluff body flows at high Reynolds number. *J. Fluid Mech.* **973**, A32.
XU, D. & ZHANG, M. 2023 Reinforcement-learning-based control of convectively unstable flows. *J. Fluid Mech.* **954**, A37.
YANG, X., GAO, C., REN, K. & ZHANG, W. 2023 Open-loop flow control design guided by the amplitude-frequency characteristics of the reduced-order model. *Phys. Fluids* **35** (12), 123612.
YAO, W. & JAIMAN, R.K. 2017 Feedback control of unstable flow and vortex-induced vibration using the eigensystem realization algorithm. *J. Fluid Mech.* **827**, 394–414.
ZHANG, M.M., CHENG, L. & ZHOU, Y. 2004 Closed-loop-controlled vortex shedding and vibration of a flexibly supported square cylinder under different schemes. *Phys. Fluids* **16** (5), 1439–1448.
ZHANG, W. & YE, Z. 2007 Reduced-order-model-based flutter analysis at high angle of attack. *J. Aircraft* **44** (6), 2086–2089.

https://doi.org/10.1017/jfm.2025.10755 Published online by Cambridge University Press

ZHAO, Y., DAI, Z., TIAN, Y. & XIONG, Y. 2020 Flow characteristics around airfoils near transonic buffet onset conditions. *Chin. J. Aeronaut.* **33** (5), 1405–1420.

ZHU, G., FANG, W. & ZHU, L. 2022 Optimizing low-Reynolds-number predation via optimal control and reinforcement learning. *J. Fluid Mech.* **944**, A3.

https://doi.org/10.1017/jfm.2025.10755 Published online by Cambridge University Press